The Dissertation Committee for Christopher Grady Rylander certifies that this is the approved version of the following dissertation:

Measurement of Transient Transport of Hyperosmotic Agents Across Cell Membranes and Resulting Optical Clearing Using Differential Phase Contrast Optical Coherence Microscopy

Committee:

_____
Kenneth R. Diller, Supervisor

_____
Ashley J. Welch

_____
Thomas E. Milner

_____
Digant P. Dave

_____
R. Malcolm Brown

_____
J. Stuart Nelson

Measurement of Transient Transport of Hyperosmotic Agents Across Cell Membranes and Resulting Optical Clearing Using Differential Phase Contrast Optical Coherence Microscopy

by

Christopher Grady Rylander, B.S.; M.S.

Dissertation

Presented to the Faculty of the Graduate School of

The University of Texas at Austin

in Partial Fulfillment

of the Requirements

for the Degree of

Doctor of Philosophy

The University of Texas at Austin

December, 2005

Dedication

To

My wife, Marissa Nichole Rylander

Acknowledgements

I want to express my sincere appreciation to my best friend and wife, Marissa Nichole Rylander, who has shared the joys and trials of our dual PhD experiences. I am proud of her recent accomplishments and excited about the adventure that lies ahead of us. I want to thank my family, for it was their guidance that led me to follow the path of graduate education. I want to thank my advisors, Dr. Ken Diller, Dr. A.J. Welch, and Dr. Thomas Milner for their guidance, wise counsel, and permission to freely direct my research course with their mentoring. I also want to thank my fellow collaborators Dr. Digant Davé, Taner Akkin, Oliver Stumpp, and Nate Kemp for their mentoring, involvement, and enthusiastic contributions to this research. This research was supported by the National Science Foundation and the Caster Foundation at The University of Texas at Austin.

Measurement of Transient Transport of Hyperosmotic Agents Across Cell Membranes and Resulting Optical Clearing Using Differential Phase Contrast Optical Coherence Microscopy

Publication No._____

Christopher Grady Rylander, Ph.D.

The University of Texas at Austin, 2005

Supervisor: Kenneth R. Diller

The response of tissue to hyper-osmotic agents is a reduction in light scattering and corresponding increase in optical clarity. "Tissue optical clearing" permits delivery of near-collimated light deeper into tissue potentially improving the capabilities of optical diagnostic and therapeutic applications. The overall objective of the proposed research is to characterize the mass transport of hyper-osmotic agents across cell membranes and the resulting optical clearing. To accomplish this task, a differential phase contrast optical coherence microscope (DPC-OCM) is configured to permit quantitative spaciotemporal optical path length (OPL) imaging of biological cell specimens.

The first application of DPC-OCM is analyzing the intracellular dry mass of individual biological cells. Differences between normal and cancerous cell dry mass are investigated. Populations of normal and cancerous human dermal fibroblast cells and human prostate cells demonstrate a statistically significant difference in mean dry mass and mean *en face* area. Linear discriminant analysis yields a maximum of 79% accurate classification.

The second application of DPC-OCM is use as a novel technique for determining cell membrane permeability parameters due to an osmotic chemical stimulus. Glycerol, a hyperosmotic agent, is perfused across an adherent layer of human keratinocytes, and the dynamic osmotic response of individual cells is imaged with DPC-OCM. A novel optical path length (OPL) mass transport model is devised relating chemical concentration to intrinsic refractive index and OPL. Hydraulic conductivity and solute permeability are determined by fitting the OPL mass transport model to transient OPL data collected with DPC-OCM.

The final study investigates the mechanisms of optical clearing of cellular and collagenous tissue using hyperosmotic agents and evaporation. OCT and photographic images quantify optical scattering reduction between native and dehydrated tissue states. Air-drying optically clears tissue as effectively as the most successful hyperosmotic agent, glycerol. Tissue ultrastructural alterations due to dehydration are investigated using transmission electron microscopy. The Rayleigh-Gans model is used to simulate light scattering effects due to tissue ultrastructural alterations and measured refractive index excursion using DPC-OCM.

Table of Contents

Chapter 1. Introduction

MOTIVATION

The response of tissue to hyper-osmotic agents reduces light scattering and thereby increases optical clarity [1-5]. This "tissue optical clearing" effect permits the delivery of near-collimated light deeper into tissue, improving the capabilities of diagnostic imaging and therapeutic applications. Optical clearing of tissue will expand the capabilities of current optical diagnostic tools such as fluorescence spectroscopy, optical coherence tomography, and confocal microscopy. Diagnostic applications that may potentially benefit include skin morphologic examination [5,6], bladder, GI, and mucosal tumor identification, and non-invasive blood glucose measurement. Laser-based therapies which may benefit from tissue clearing include treatment of Port Wine Stain, hair removal, ablation of deep stromal tumors, leg vein coagulation, photodynamic therapy of tumors, targeting of individual dermal vessels, transscleral photocoagulation, and endoscopic surgery of the bladder, prostate, and GI tract.

Based on original research at The University of Texas at Austin, the primary mechanisms of light scattering reduction in skin are (1) dehydration and (2) refractive index matching between the tissue constituents and the hyper-osmotic agent [1-5]. Other research at Beckman Labs (UC Irvine) suggests that the structural change of collagen molecules is the primary mechanism of reduced light scattering in skin [7]. All of these effects result from the transient transport of water and hyper-osmotic agent in response to a chemical concentration imbalance. Investigation of the transport process is necessary

to understand and design protocols to enhance the outcome of tissue optical clearing. The research focuses on cell membrane transport and optical clearing at the cellular level.

The proposed research is of great interest for its intrinsic scientific value in the field of biological mass transport. The newly developed technology of DPCOCM provides a novel method for visualizing and quantifying the mass transport of osmotically active chemical species across cell membranes. It allows simultaneous measurement of the chemical forces and flows driving the transport process. Biological transport applications extend into the fields of cryobiology and tissue engineering. Development of the DPCOCM system will facilitate its use in other applications such as quantitative cytology [8-10] and micro-scale heat transfer measurements.

This research contributes to increased understanding of the mechanisms of tissue clearing by correlating changes in optical properties with transport effects occurring at the cellular level. Calculated cell membrane permeability parameters and correlation between agent concentration and refractive index may be used to design an optimal cellular clearing protocol (prescribed concentration of each agent) for each cell type.

OBJECTIVES

The overall objective of the proposed research is to characterize the mass transport of hyper-osmotic agents across cell membranes and the resulting optical clearing. Mass transport is quantified by measuring transient hyper-osmotic agent concentration differentials across cell membranes, measuring transient cell volume excursion, and calculating cell membrane permeability parameters. Optical clearing is

quantified by measuring transient refractive index matching of hyper-osmotic agents to cell organelles and calculating the reduced scattering cross coefficient, μ_s'. Studies are conducted using experimental and theoretical techniques. The following set of specific aims is designed to achieve this objective:

1. Configure a Differential Phase Contrast Optical Coherence Microscope (DPCOCM) to allow quantification of spaciotemporal refractive index within and surrounding single cells during perfusion of hyper-osmotic agents.
2. Quantify the transient hyper-osmotic agent concentration differentials across cell membranes using DPCOCM measured refractive index.
3. Quantify the transient volume excursion of cells in response to hyper-osmotic stress using DPCOCM cell image area and appropriate geometry.
4. Calculate cell membrane permeability parameters to various hyper-osmotic agents by fitting the membrane transport model to experimentally measured hyper-osmotic agent transmembrane concentration differentials and the associated transient cell volume excursion.
5. Calculate the transient σ_s' of individual cells due to the simultaneous effects of cell dehydration and refractive index matching using Rayleigh-Gans scattering theory.

The aforementioned specific aims are diagrammatically represented in figure 1.1. This figure reveals the coupling between the mass transport studies (top branch) and the

optical property studies (bottom branch). It also illustrates the mixture of experimental (ovals) and theoretical (squares) techniques used to achieve the objective.

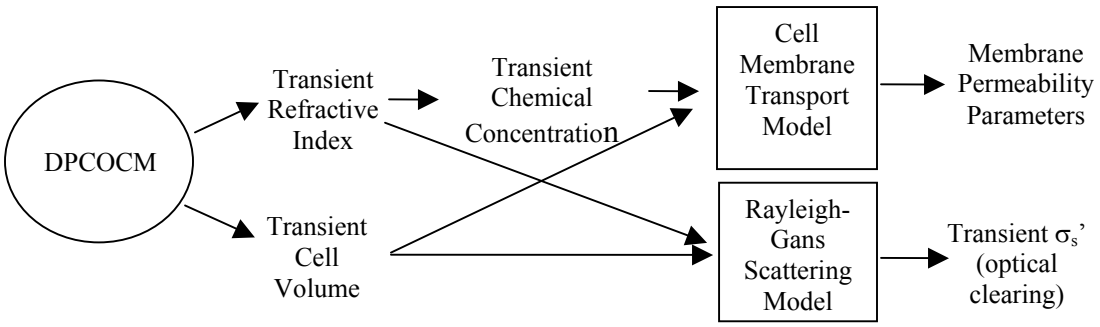

Figure 1.1. Diagram representing the interconnectedness of specific aims.

DISSERTATION OVERVIEW

Chapter 2 describes the configuration of a differential phase contrast optical coherence microscope (DPC-OCM), which permits quantitative spaciotemporal optical path length (OPL) imaging of biological cell specimens. The system has 1 nm OPL resolution, and 1 μm lateral resolution. Comparison is made between two different configurations of sample path optics. Chapter two was published in *Optics Letters* in July 2004. Two example applications of DPC-OCM are presented in chapters three and four.

Chapter 3 describes application of DPC-OCM for analyzing the intracellular dry mass of individual biological cells. Differences between normal and cancerous cell dry mass are investigated. Populations of normal and cancerous human dermal fibroblast cells and human prostate cells demonstrate a statistically significant difference in mean dry mass and mean *en face* area. Linear discriminant analysis yields a maximum of 79% accurate classification. The content of chapter three is intended for publication as a letter

or research report in a cancer research journal such as *Cancer Detection and Prevention* or *Cancer Cytopathology*.

Chapter 4 presents a novel technique for determining cell membrane permeability parameters due to an osmotic chemical stimulus. Glycerol, a hyperosmotic agent, is perfused across an adherent layer of human keratinocytes, and the dynamic osmotic response of individual cells is imaged with DPC-OCM. A novel OPL mass transport model is devised relating chemical concentration to intrinsic refractive index and OPL. Hydraulic conductivity and solute permeability are determined by fitting the OPL mass transport model to transient OPL data collected with the DPC-OCM. The content of chapter four is intended for publication in *Journal of Biomechanical Engineering*.

Chapter 5 investigates the dehydration mechanism of optical clearing of cellular and collagenous tissue using hyperosmotic agents and evaporation. OCT and photographic images quantify optical scattering reduction between native and dehydrated tissue states. Air-drying optically clears tissue as effectively as the most successful hyperosmotic agent, glycerol. Tissue ultrastructural alterations due to dehydration are investigated using transmission electron microscopy. The Rayleigh-Gans model is used to simulate light scattering effects due to tissue ultrastructural alterations. The content of chapter five is intended for publication in *Journal of Biomedical Optics*.

BACKGROUND

Transport of Hyper-osmotic Agents Across Cell Membranes

The hyper-osmotics are a category of drugs clinically used to move water from

the intracellular to the intravascular space. Medically useful hyper-osmotic agents include the polyhydric alcohols like glycerol and ethylene glycol and the linear alcohols like sorbitol and mannitol. Other examples include hypaque, dimethyl sulfoxide (DMSO), polyethylene glycol, and sucrose.

In general, cell membranes have a lower permeability to hyper-osmotic agents than to water. The osmotic stress produced by the agent in the extracellular space causes an initial flux of intracellular water out of the cell faster than the hyper-osmotic agent penetrates the cell. This results in an initial decrease in cell volume followed by a more gradual swelling as the hyper-osmotic agent accompanied by water enters the cell [11-14]. As trans-membrane equilibrium is approached, the net transport process diminishes. These events (Figure 1.2) may occur in a matter of seconds to minutes depending on the plasma membrane water and solute permeability.

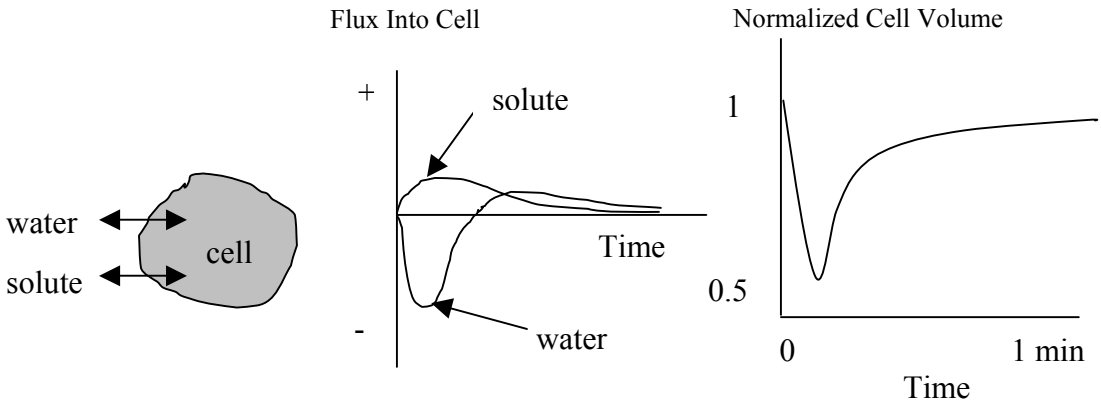

Figure 1.2. (a) Single cell biophysical system representing the transport of water and hyper-osmotic agent (solute). (b) Transient solute and water flux and (c) resulting cell volume due to application of a hyper-osmotic agent.

Refractive Index and Concentration

The refractive index of a binary solution is related to the concentration of solute, temperature, and wavelength of interrogating light [15]. Provided the temperature and wavelength are known and fixed, solute concentration can be determined from the measured refractive index. The Lorentz-Lorenz formula [16,17] relates the effective refractive index, n, of a mixture of substances in the following manner:

$$\frac{n^2 - 1}{n^2 + 2} = \sum_i A_i C_i \tag{1.1}$$

where A and C are the molar refractivity of substance i and the number of moles of substance i per unit volume, respectively.

Alternatively, the specific refractive increment (α) of a solution can be used to relate refractive index and concentration for solutions, such as glycerol, that exhibit a near-linear relationship between these parameters. The specific refraction increment of a solution is defined as the increase in refractive index for every 1% increase in concentration of the solute.

$$\alpha = \frac{dn}{dC} \tag{1.2}$$

The specific refractive increment for a given protein solution remains constant over a fairly wide range of concentrations (up to at least 45% for bovine serum albumin) provided the concentration (C) is expressed in terms of grams per 100 mL of solution. The refractive increment of nearly all soluble unconjugated proteins falls within .0018

±2% at 20^{O}C in green or yellow light [18]. Therefore the concentration of protein in a cell immersed in water can be expressed as:

$$C = \frac{(n - 1.333)}{.0018} \tag{1.3}$$

Mechanisms of Tissue Optical Clearing

The complex shape, size, and distribution of tissue constituents, as well as variations in the index of refraction, provides a highly scattering medium for visible and near infrared light. In addition to water (n=1.33), a wide range of refractive indices are associated with cellular constituents (Table 1.1).

Table 1.1 Index of refraction values for cellular constituents.

Cell Component	Refractive Index	Wavelength	Technique	Reference
extracellular fluid	1.35	850 nm	Light Scattering	[19] Maier et al.
cytoplasm	1.37	Visible	Interference Microscopy	[20] Barer et al.
nucleus	1.39	Visible	Interference Microscopy	[21] Barer et al.
mitochondria	1.42	780 nm	Light Scattering	[22] Beauvoit et al.

The addition of solutes to tissue affects the global optical properties by causing changes in cell morphology and refractive index of the extracellular and intracellular spaces [11-14]. Refractive index gradients evolve transiently as water is transported out of the cells/tissue and the applied agent is transported in. Moreover, as water is removed from the tissue the concentration of salts and proteins in the tissue rises, increasing the refractive index of the extracellular space and possibly the intracellular space. Depending on the degree of refractive index matching and changes in cell size, a reduction in light scattering may occur.

Skin Structure

The skin is the largest organ of the body. This structure has many important roles including: providing a protective barrier to the environment, permitting sensation and thermoregulation, and metabolic functions. The skin anatomy is depicted in figure 1.3. The epidermis is the most exterior layer, and is approximately 60-80 μm in thickness. The epidermis is comprised of five layers in order of the most superficial to the most interior layers: stratum corneum, stratum lucidum, stratum granulosum, stratum spinosum, and the stratum germinatum [23]. The most superficial layer of the epidermis is the stratum corneum. This layer is responsible for preventing entry of foreign intruders into the skin. The primary cell type in the epidermis is the keratinocyte. Due to their important role in barrier function, the measurement of glycerol transport in these cells will be discussed in the dissertation. The skin layer below the epidermis is termed the dermis. This layer comprising 1-2 mm in humans, is composed of a network of elastic and collagen fibers, ground substance consisting of glycosaminoproteoglycans, salts, proteins, and water. Fibroblasts are the major cell of the dermis and secrete structural proteins such as collagen, elastin, and ground substance in order to provide support and skin elasticity. [23,24]. The dermis is comprised of two layers: the reticular and papillary dermis for which collagen is a major component. The reticular dermis comprises the majority of the dermis and provides the skin with strength and elasticity. Within this layer collagen bundles are very tightly packed and there is very minimal ground substance. Elastic fibers which are composed of microfibrils (10 to 12 μm in diameter) reside in an amorphous elastin matrix through which the collagen fibers are

interwoven. The papillary dermis contains the vasculature which provides nutrients and permits thermoregulation. The collagen fibers are loosely distributed in the papillary dermis and range in diameter from .3 to 3 μm. A subcutaneous fatty tissue layer exists below the dermis. A muscle layer resides below the fatty layer in hamsters, rats, and in the facial skin of humans. The skin is also composed of essential structures such as hair follicles, nerves that sense heat, pain, pressure, cold, and touch, sebaceous glands that secrete lubricating sebum, and sweat glands that produce perspiration.

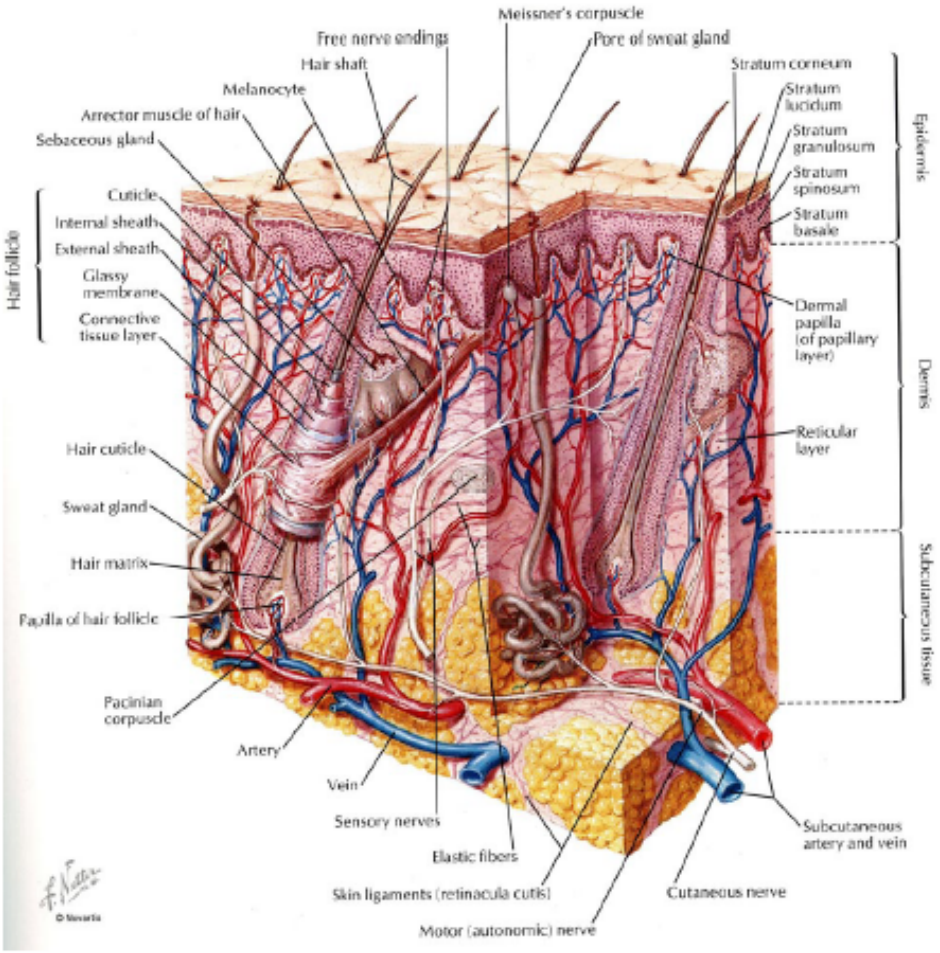

Figure 1.3. Skin anatomy [25].

Chapter 2. Quantitative Phase Contrast Imaging of Cells with Phase Sensitive Optical Coherence Microscopy[1]

ABSTRACT

We describe a method for *en face* phase contrast imaging of cells with a fiber-based differential phase contrast optical coherence microscopy system. Recorded *en face* images are quantitative phase contrast maps of cells due to spatial variation of refractive index and/or thickness of various cellular components. Quantitative phase contrast images of human epithelial cheek cells obtained with the fiber-based DPC-OCM system are presented.

[1] Portions of this chapter have been previously published in *Optics Letters* [39].

INTRODUCTION

Phase contrast microscopy (PCM) is a powerful tool for visualization of unstained biological specimens. Traditional PCM techniques such as differential interference contrast (DIC) and Zernike phase contrast do not provide a direct quantitative measure of the spatially varying phase in a biological specimen such as a cell. Many functional imaging applications of unstained cells require quantification of subtle phase contrast changes in a cell with sub-cellular resolution. These applications include fundamental studies of cell membrane dynamics in response to chemical stimuli, quantitative pathology of cells for disease diagnosis and staging, and imaging of unstained tissue samples. Optical contrast in cells arises primarily due to spatial refractive index gradients among cellular components. Variations in refractive index and geometric size of cellular components contribute to the total phase contrast, i.e. the composite spatial optical path length (OPL) variation in a biological specimen. Methods and techniques developed for quantitative phase contrast imaging of cells include numerical reconstruction of phase information from DIC images [26,27], interference microscopy, and digital holography [28]. Recently, direct measurement of optical path length changes in transparent and turbid samples with nanometer sensitivity has been demonstrated using phase-sensitive low-coherence interferometry (PS-LCI) [29-34]. Compared to other quantitative phase contrast imaging techniques, PS-LCI has the advantage that it permits direct quantitative measurement of depth resolved phase contrast with high sensitivity in reflection mode. Although phase information is readily available in the recorded interference fringe intensity signal in a single channel LCI, values are corrupted with phase noise (on the

order of a radian) due to environmental perturbations rendering it unsuitable for high resolution quantitative phase-contrast imaging. High phase sensitivity is achieved by canceling common-mode phase noise in a dual (polarization or wavelength) channel interferometer.

MATERIALS/METHODS

In this letter we describe the implementation of a fiber-based PS-LCI as a differential phase contrast optical coherence microscope (DPC-OCM) [31] for high-resolution quantitative phase contrast imaging of cells. The fiber-based DPC-OCM provides flexibility in interrogating a variety of samples and is well suited for biomedical applications requiring in vivo imaging.

The fiber-based DPC-OCM (Figure 2.1) is a dual-channel low-coherence Michelson interferometer capable of measuring sub-wavelength optical path length difference between light backscattered from two spatially separated sites in a sample [33,34]. Light emitted from an optical semiconductor amplifier (centered at λ_o=1.31 μm; FWHM spectral bandwidth, $\Delta\lambda$=60 nm; free space coherence length of 22 μm) is coupled into the input port of a polarization-maintaining (PM) coupler. The two channels of the low-coherence interferometer correspond to orthogonal and decorrelated polarization modes of the PM fiber. Decorrelation of the two polarization modes is an important feature of the DPC-OCM system as it ensures that cross-coupled light from one channel to the other does not contribute to the interferometric signal in either channel. The two channels constitute the two probe beams incident on a sample and are referred to as Channel 1 (Ch1) and Channel 2 (Ch2). At the 2x2 PM coupler, each channel is split equally into reference and sample arms.

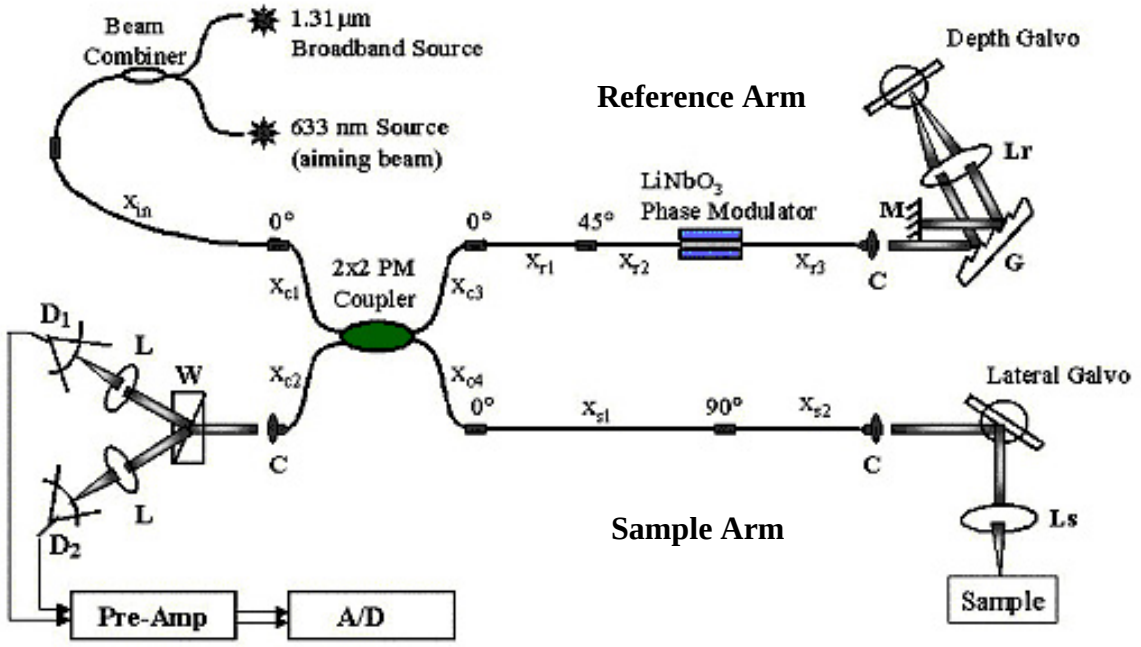

Figure 2.1. Schematic diagram of the DPC-OCM. Details of the system are presented in references 43 and 44.

The reference arm incorporates a $LiNbO_3$ electro-optic phase modulator that permits stable phase modulation and accurate measurement of fast transient differential phase changes. The dispersion compensating delay line consists of a diffraction grating, "G", that compensates for chromatic and waveguide dispersion introduced by the phase modulator. Depth scans (A-scans) are possible by modulation of the depth galvo mirror angle, but are not performed during data collection since the maximum sample retardation (1000 nm) is well within the coherence length of the source.

Sample path optics are configured with two different geometries described in detail later. Common to both geometries are two galvos which enable scanning in two lateral dimensions. Two birefringent prisms enable lateral or axial separation of probe

beams. A 40× microscope objective, "Ls", (N.A=0.6) is used to focus the probe beams on the sample.

Back reflected light from the reference and sample path in Ch1 and Ch2 mix at the PM coupler to form interference fringe intensity signals (I_m, $m=1,2$). In the detector path, polarization channels are separated by a large angle Wollaston prism, "W", and focussed on to respective photoreceivers, "D_1" and "D_2". The interference signal is digitized using a 12 bit analog-to-digital converter, "A/D". Interference fringe intensity signal formed in each channel is given by

$$I_m(z) = 2I_o\sqrt{R_{ref}R_{samp}(z)}\left\{\exp\left[-(z-z_o)/l_c\right]^2\right\}\left\{\cos(2\pi f_o t + \varphi_m + \varphi_{noise})\right\} \qquad (2.1)$$

where I_o is a scale factor with units of intensity, source coherence length (l_c) is 22 μm, R is reflectivity in reference (R_{ref}) and sample (R_{samp}) paths, f_o is the phase modulation frequency, φ_{noise} is the common mode phase noise in the interferometer due to stochastic environmental perturbations, and $\varphi_m(z)$ ($m=1$ or 2) is the phase term that carries relevant specimen information. Using Hilbert transform $\mathcal{H}(.)$, phase of interference fringe intensity signal in each channels is determined. Phase function of the interference fringe intensity signal in Eq. 2.1 is given by

$$\varphi_m = arc\tan\left\{\frac{\mathcal{H}(I_m)}{I_m}\right\} \qquad (2.2)$$

In a differential phase measurement, $\Delta\varphi$ is proportional to difference in optical path-length (Δp) traversed by light in Ch1 and Ch2:

$$\Delta\varphi = 2\left(\frac{2\pi}{\lambda_o}\right)\Delta p \tag{2.3}$$

A factor of two in Eq. 2.3 accounts for the double pass geometry. Δp is a function of refractive index variation (Δn) and physical path length difference, l, between Ch1 and Ch2 and can be written as

$$\Delta p = \int \Delta n(l)dl \tag{2.4}$$

The fiber-based DPC-OCM has a differential phase measuring accuracy better than 0.05 radian (OPL ~ 5 nm). Optical path length measuring accuracy of the fiber-based DPC-OCM is verified by scanning the height of a chromium nano-step (Figure 2.2). The chromium nano-step is mounted on a computer controlled linear translation stage and scanned laterally. Height profiles of the chromium nano-step measured with DPC-OCM (150 nm) and an atomic force microscope (155 nm) match within 5 nm.

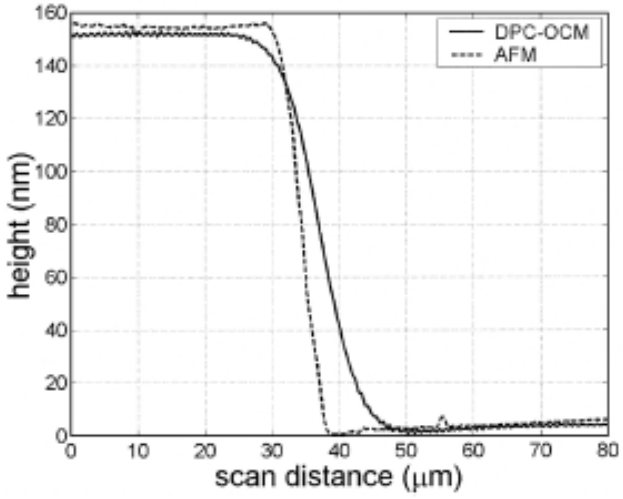

Figure 2.2. Height profile of the chromium nano-step measured with prototype DPC-OCM system and an atomic force microscope.

We describe two probe beam geometries for *en face* quantitative phase-contrast imaging of single layered cells. Choice of probe beam configuration for *en face* imaging of cells depends on the application. The sample holder and two configurations of sample path optics to spatially separate Ch1 and Ch2 are shown in Figure 2.3. The cells are positioned between two glass cover slips that served as a sample holder (Figure 2.3a). Prior to *en face* DPC-OCM imaging, cells are first visualized using an inverted microscope with the objective positioned beneath the sample holder. Observation of the DPC-OCM aiming beam in the inverted microscope image allows co-registration of recorded images. Intensity interference signals in Ch1 and Ch2 are recorded while raster scanning (xy-plane) the probe beams over the sample.

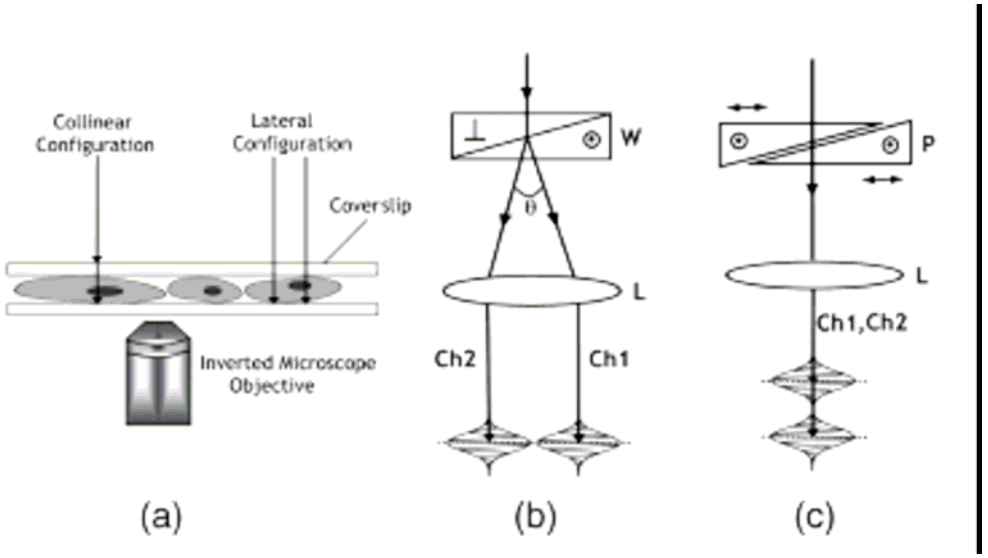

Figure 2.3. (a) Sample path configuration for recording brightfield and *en face* DPC-OCM images. Lateral (b) and collinear (c) configurations of sample path optics to spatially separate probe beams. In the lateral configuration, Wollaston (W) prism and specimen are positioned in front and back focal planes of lens (L), respectively. In the

collinear configuration, translation of birefringent prism pair (P) allows variation of optical pathlength difference between Ch1 and Ch2. Optical axis (⊥ or ●) of birefringent elements in lateral and collinear configurations is indicated.

In the lateral configuration (Figure 2.3b), a Wollaston prism laterally splits light in Ch1 and Ch2 and a lens focuses and makes parallel the orthogonally polarized probe beams incident on the specimen. Magnitude of lateral spatial separation between Ch1 and Ch2 is dependent on the divergence angle of the Wollaston prism and sample path focusing optics. For cell imaging using the lateral configuration, the two probe beams are focused at the water-glass interface of the bottom cover-slip (Figure 2.3a) to record an image. At a given depth (z_o) and lateral position (y_o), "raw" phase difference [$\Delta\varphi(x,y_o,z_o)=\varphi_2(x+\Delta x,y_o,z_o)-\varphi_1(x,y_o,z_o)$] between the two probe beams in Ch1 and Ch2 along the line scan in *x*-dimension is given by

$$\Delta\varphi(x,y_o)=\frac{4\pi}{\lambda_o}\int_0^{z_o}\left[n(x+\Delta x,y,z)-n(x,y_o,z)\right]\cdot dz=\frac{4\pi\cdot\Delta x}{\lambda_o}\int_0^{z_o}\left[\frac{\partial n(x,y_o,z)}{\partial x}\right]\cdot dz \qquad (2.5)$$

Inasmuch as the probe beams are laterally separated by Δx, the "raw" phase-difference (Δφ) represents a gradient with respect to x of optical path length change.[7] True phase difference (Ψ) representative of the physical structure due to optical path length variation for each lateral line scan is obtained by integrating Eq. 2.5:

$$\Delta\Psi(x,y_o)=\frac{1}{\Delta x}\int\Delta\varphi(x,y_o).dx \qquad (2.6)$$

In the collinear configuration (Figure 2.3c) Ch1 and Ch2 are laterally coincident but axially separated. Translating the birefringent prisms laterally (x-direction) with respect to each other varies the axial separation between Ch1 and Ch2. While imaging cells using the collinear configuration, the probe beams are positioned at the top surface of each cover slip and the phase difference between the channels is given by

$$\Delta\varphi(x, y_o) = \frac{4\pi}{\lambda_o}\left\{\int_0^{z_o} n(x, y_o, z)\cdot dz - n_{glass}t_{glass}\right\} \qquad (2.7)$$

where n_{glass} and t_{glass} are refractive index and geometric thickness of the cover slip, respectively.

RESULTS

Recorded *en face* DPC-OCM images of human epithelial cheek cells are shown in Figure 2.4 and Figure 2.5. Human epithelial cheek cells were prepared by gently swabbing the inner cheek of a volunteer with a cotton tip and placing the specimen in a drop of water on a glass slide. A 40× microscope objective (N.A=0.6) is used to focus the probe beams on the sample. FWHM of probe beam at the focus is approximately 3.5 μm. In the lateral beam configuration the beam separation is approximately 5 μm. Recorded DPC-OCM *en face* images of single epithelial cells using the two configurations with corresponding bright field are shown are shown in Figure 2.4. DPC-OCM images are recorded using a scanning mirror and motorized linear translation stage in case of the collinear beam configuration, whereas two motorized linear translation stages were used for the lateral beam configuration. Sample holder is placed on the motorized linear translation stage. It takes a couple of seconds to record an image with the collinear configuration but more than a minute with the lateral configuration due to the limited speed of the translation stages. Faster image acquisition can be achieved for both configurations by using two scanning mirrors and optimized flat field scanning optics. Poor reflectivity/absorption contrast of epithelial cheek cells makes visualization difficult with a bright field microscope. Under oblique transillumination epithelial cells can be visualized, though not with corresponding clarity as can be obtained with a phase-contrast microscope.

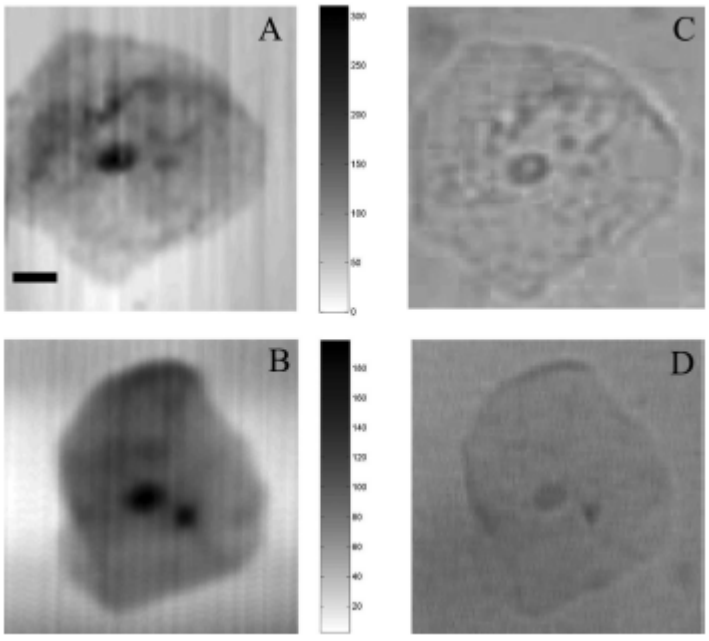

Figure 2.4. DPC-OCM (a & b) and bright field microscope images (c & d) of single human epithelial cheek cells. Lateral (a) and collinear (b) probe beam configuation were used to record DPC-OCM images. Color bar denotes single pass optical path length difference in nanometers. (Scale bar – 10 μm)

DPC-OCM image of multiple epithelial cheek cells recorded using the collinear configuration is compared with a phase-contrast microscope image of similar epithelial cells (Figure 2.5). The phase contrast image shown is not of the same epithelial cells since it is not possible to record DPC-OCM and phase-contrast microscope images simultaneously with our setup. Cell wall, nucleus and some other sub-cellular features are visible in DPC-OCM images of epithelial cheek cells. *En face* DPC-OCM images quantitatively map the variation of optical path length in epithelial cheek cells. Lateral

resolution of DPC-OCM can be improved by optimizing the sample path focusing optics and operating at a lower wavelength.

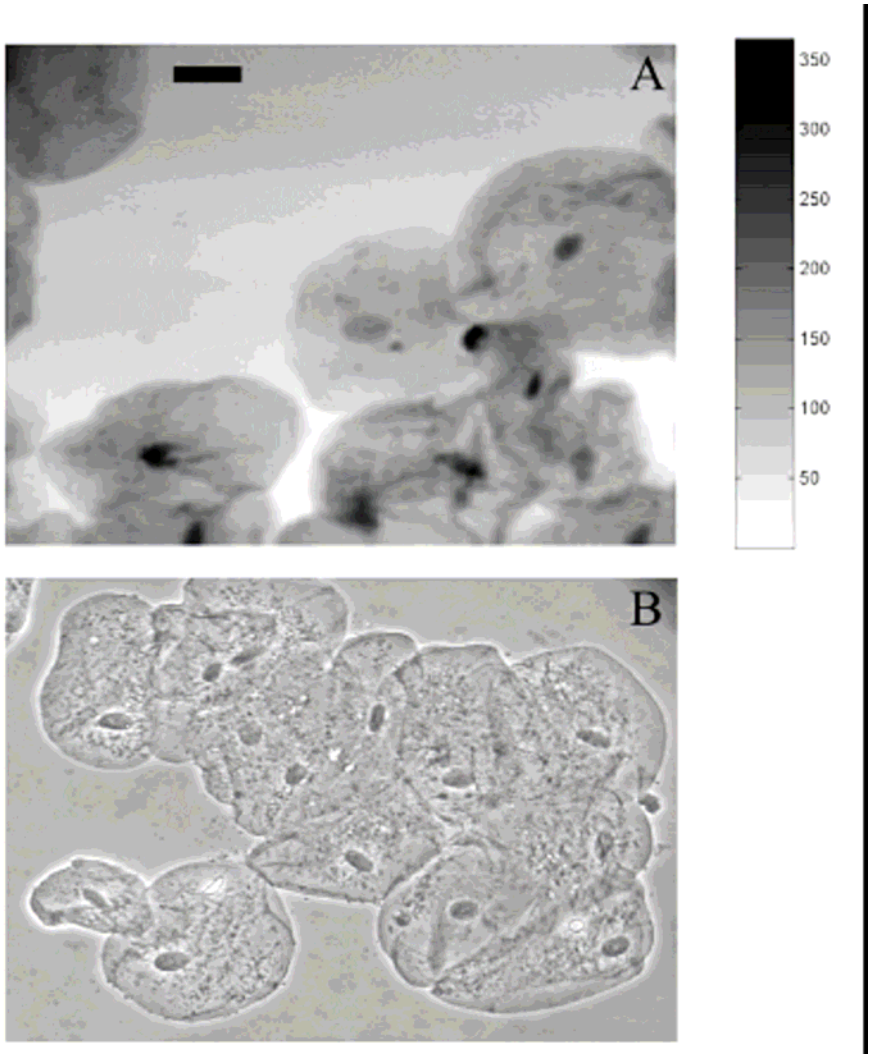

Figure 2.5. DPC-OCM (a) and phase-contrast microscope image (b) of multiple human epithelial cheek cells. The images are of similar epithelial cells but not the same sample. Color bar denotes single pass optical path length difference in nanometers. (Scale bar – 20 μm)

If a transparent flat reference surface above the cells is available, the collinear configuration is more suitable for quantitative phase contrast imaging since the optical setup is simpler, phase sensitivity and accuracy of calculated differential phase contrast is higher. With the lateral configuration probe beam configuration only a single reflecting surface below the cell layer is necessary which is easily available since cells are either grown or placed on glass cover slips. Construction of accurate quantitative DPC-OCM images using the lateral configuration requires accurate knowledge of probe beam separation in the specimen. Since the probe beams are orthogonal polarized, birefringence in the cell will also contribute to the phase difference.

CONCLUSION

In conclusion, we have demonstrated a fiber-based DPC-OCM that is capable of recording quantitative phase contrast images of individual cells with sub-cellular resolution. Because the DPC-OCM can record transient changes in optical path length, the system may be used to record quantitative optical path length alterations of cells in response to various stimuli. Results of studies of optical path length change of cells in response to chemical and other stimulus will be reported subsequently. A fiber-based DPC-OCM has the potential to substantially improve in vivo imaging of epithelial tissues for a variety of clinical diagnostics and monitoring applications. Depth-resolved quantitative phase contrast imaging of a multilayered and complex structure such as tissue is challenging because a reference surface may not be readily available. Experiments are underway using both probe beam configurations described above to record depth-resolved quantitative phase contrast images of tissue.

Chapter 3. Measurement of Total Cell Dry Mass using Differential Phase Contrast Optical Coherence Microscopy to Discriminate Normal and Cancerous Cell Populations

ABSTRACT

Differential phase contrast optical coherence microscopy (DPC-OCM), a quantitative imaging technique, was used to measure *en face* area and dry mass of normal and cancerous populations of human fibroblast and prostate cells. There was a significant difference ($p>0.05$) between normal and cancer population averages of dry mass and area. However, the use of linear discriminant analysis was 75-79% accurate at best. Mass was a better classifier than area for both cell types. Advantages and disadvantages of the DPC-OCM instrument are discussed as is the concept of using dry mass a discriminant parameter to classify normal and cancerous cell populations.

INTRODUCTION:

Early, preinvasive cancer cells are readily treatable, but difficult to detect. Beginning in the preinvasive stage known as dysplasia, cell architecture is altered. Specifically, cell nuclei become enlarged, crowded, and hyperchromatic (staining abnormally dark with a contrast agent due to changes in their chromatin content) [35]. The dry mass of dysplastic cell nuclei is higher than that of normal cells, although mass concentration is less [36].

We have shown that the dry mass (protein content) of entire cancerous cells is elevated relative to normal cells and therefore has the potential to be used as an indicator of the presence of cancer. Interference microscopy has been applied to measure cell dry mass since the early 1950s [37]. A novel technique known a DPC-OCM has the same phase sensitive capabilities as interference microscopy, and possesses several benefits over the former, most importantly it has the potential to be applied *in vivo*.

Interference microscopy and DPC-OCM detect the phase retardation induced when a beam of light passes through a specimen. The amount of retardation depends on the specimen concentration and physical thickness. The optical path length (Φ) measured across a chamber (physical thickness z_2-z_1) containing a cell is the integral product of refractive index (n) and differential thickness (dz) of the chamber (Equation 3.1, Figure 3.1a).

$$\Phi = \int_{z'=z_1}^{z_2} n(z')dz' \qquad (3.1)$$

The optical path length integrated over the cell *en face* area (A) (Figure 3.1b) results in an effective "optical volume." The optical volume divided by A defines the spatial average optical path length over the intracellular region, Φ_{in} (Equation 3.2).

$$\Phi_{in} = \frac{1}{A}\int_{A} \Phi \cdot dA \tag{3.2}$$

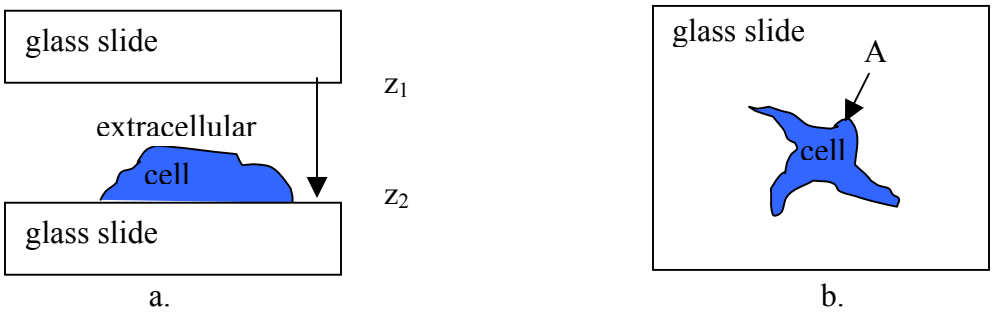

Figure 3.1. a) Side and b) top view of the chamber containing the cell (shaded).

Φ_{in} is dependent on the total chemical composition and volume of the cell, and independent of cell shape. Unfortunately, it is also dependent on the chemical composition and volume of extracellular medium between the cell boundary and the "control volume" boundary. In order to preserve the former mentioned benefit and alleviate the latter mentioned consequence of Φ_{in}, the effect of the extracellular medium must be removed. The differential optical path length ($\Delta\Phi$) is calculated by subtracting the extracellular optical path length (Φ_{ex}) from Φ_{in} (Equation 3.3).

$$\Delta\Phi = \Phi_{in} - \Phi_{ex} \tag{3.3}$$

The mass of dry substance, M, within the cell is given by Equation 3.4 where α is the specific increment in refractive index for the solute and the refractive index of the extracellular immersion medium is chosen equal to water (n=1.333).

$$M = \frac{\Delta\Phi \cdot A}{100 \cdot \alpha} \tag{3.4}$$

The specific increment is determined by the molecular polarizability due to the interaction between light and the solute molecules. The α for cells is determined mainly by proteins and nucleic acids, and its value may be taken as 0.0018 cm^3/g. Specific increment is independent of protein concentration for concentrations up to 50%, and only slightly dependent on salt and protein molecular weight [37].

MATERIALS/METHODS:

Φ Imaging Using DPC-OCM

DPC-OCM is an imaging technique capable of quantifying ΔΦ and cell dry mass [34,38,39]. The sample path optics are configured for the specific cell sample preparation as shown in Figure 3.2. Cells are cultured on a glass coverslip and a second glass coverslip is applied above the cells. Four birefringent prisms are used to induce a relative path-length delay between the two orthogonal polarization channels. In this manner, the Ch2 interferogram produced by the glass interface above the cell is temporally retarded (axially separated) to occur simultaneously with the Ch1 interferogram produced by the glass interface below the cell. The Ch2 interferogram acts as a reference while the Ch1 interferogram passes through the cellular sample and extracellular medium, acquiring relevant specimen information. The two coaxial channels (no lateral separation) are reflected off two scanning mirrors and directed through a high-numerical-aperature (N.A.=1.4) 40X microscope objective, producing a 3 μm FWHM beam diameter in the focal plane. The focal plane corresponds with the center of the chamber.

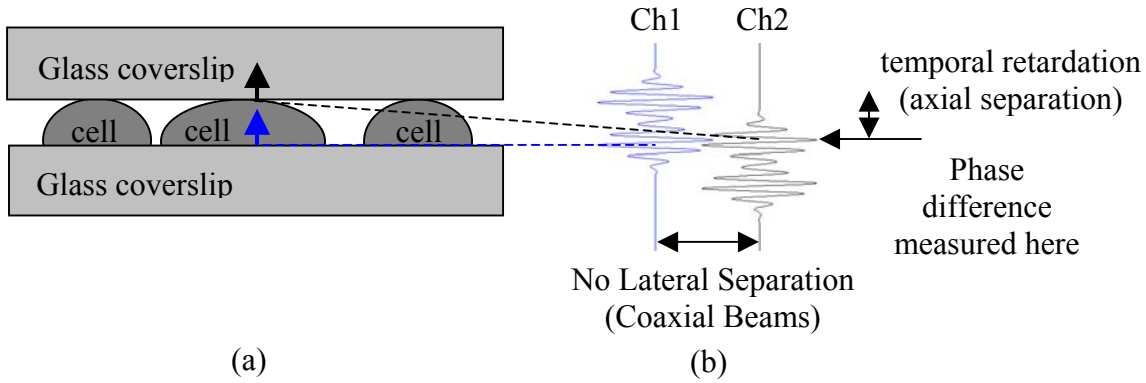

Figure 3.2. (a) Side-view schematic representation of sample preparation. Arrows represent backreflected light which is simultaneously interfering. (b) A-scans reveal the light amplitude reflected from the two glass slides and thus provide feedback for focusing and adjusting the temporal delay (axial separation) between the two channels.

Phase difference between the two channels, $\Delta\phi=\phi_2-\phi_1$, rejects common-mode phase noise present in both channels. Relative optical path length ($\Phi(x,y)$) can be calculated from phase difference with 1 nm resolution by:

$$\Phi(x,y)=\frac{\Delta\phi(x,y)\cdot\lambda_c}{4\pi} \tag{3.5}$$

Cell Sample Preparation

Normal (RWPE) and cancerous (PC3) prostate cells and normal (CCL-171) and cancerous (CCL-121) fibroblast cells were cultured according to the protocol specified by ATCC [40]. Glass coverslips were sterilized in alcohol and coated with poly-l-lysine to allow cell adhesion. Cells were immersed in fresh minimal essential medium (Gibco 11095-098) every three days and incubated at 37 ^{o}C with a 5% CO_2 in air atmosphere.

Two subculture procedures (two passages) were performed prior to experimentation. Samples were imaged when cells reached approximately 25% confluence. Individual optical flats and adherent cells were rinsed with isotonic saline solution to remove debris immediately prior to experimentation. Approximately 3-4 glass coverslips provided all specimens for each combination of cell state and type.

Data Processing and Analysis

Cell *en face* area (A) was determined using manual edge-detection of the cell perimeter in the digital Φ images. Φ_{in} was calculated by averaging the values of Φ within the A boundary. Φ_{ex} was calculated by averaging Φ within a region of interest selected adjacent to the cell. Cell dry mass was calculated using Equations 3.3 and 3.4.

Several statistical measurements were performed on normal (n=272) and cancer (n=272) prostate cells and normal (n=288) and cancer (n=288) fibroblast cells. First, population mean and standard deviation were calculated for area and mass corresponding to a specific combination of cell type (prostate/fibroblast) and cell state (normal/cancer). Histograms were plotted for each cell type and state by dividing area and mass into 30 evenly spaced bins ranging from 0 to 1500 um^2 and picograms, respectively. Comparisons were made between the normal and cancerous states for each cell type.

Next, the Lilliefors test for goodness of fit to a normal distribution [41] was applied to each histogram. The Lilliefors test evaluates the hypothesis that the sample population could have come from a normal distribution with unspecified mean and variance in terms of rejecting the null hypothesis that the populations have normal

distributions. This test compares the sample distribution of each histogram with a normal distribution having the same mean and variance. The null hypothesis is rejected if the test is significant at the 5% level.

The Wilcox rank-sum test [41] was performed for area and mass parameters of each cell type to determine whether the normal and cancer cell populations were identical. The Wilcox rank-sum test evaluates the hypothesis that the two populations are not significantly different. The null hypothesis is rejected if the test is significant at the 5% level. P is the probability of observing a result equally or more extreme than the one using the data (normal and cancer) if the null hypothesis can not be rejected.

Next, a linear discriminant analysis (LDA) [42] was performed separately for prostate and fibroblast data using all of the experimental samples. The Bayes classifier computes discriminant scores to determine the group into which each sample is classified. The training set for LDA was taken to be the entire experimental data set.

Finally, cross correlation coefficients between area and mass parameters were determined for each cell type and state. A cross correlation value of 0 indicates no correlation, while a value of 1 indicates perfect correlation.

RESULTS

DPC-OCM images of normal and cancerous human prostate cells are shown in Figure 3.3. The field of view is 100 μm x 100 μm. The value of Φ [nm] at each spatial position is specified by its grayscale intensity.

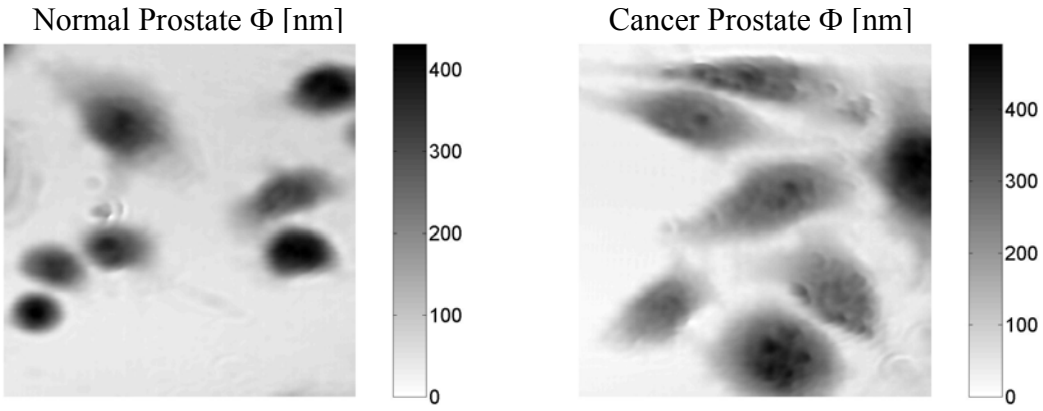

Figure 3.3. Example images of normal (left) and cancerous (right) human prostate cells. (100 μm x 100 μm field of view)

Histograms comparing normal and cancer cell area and mass for both cell types are presented in Figure 3.4. The area and mass population average and standard deviation for each cell type and state is presented in Table 3.1. Both area and dry mass population averages are greater in the cancerous versus normal state for prostate cells. This observation is also true of fibroblast mass, but not area. Total percentage of accurately classified cells was defined as percentage of normal cells whose area (or mass) was less than a cutoff value and cancer cells whose area (or mass) was greater than the same cutoff value. The maximum percentage of accurately classified cells and

corresponding cutoff values are plotted as a vertical dashed line in Figure 3.4. Using the total percentage of accurately classified cells as an indicator of classifier effectiveness, mass is a better classifier than area for both cell types.

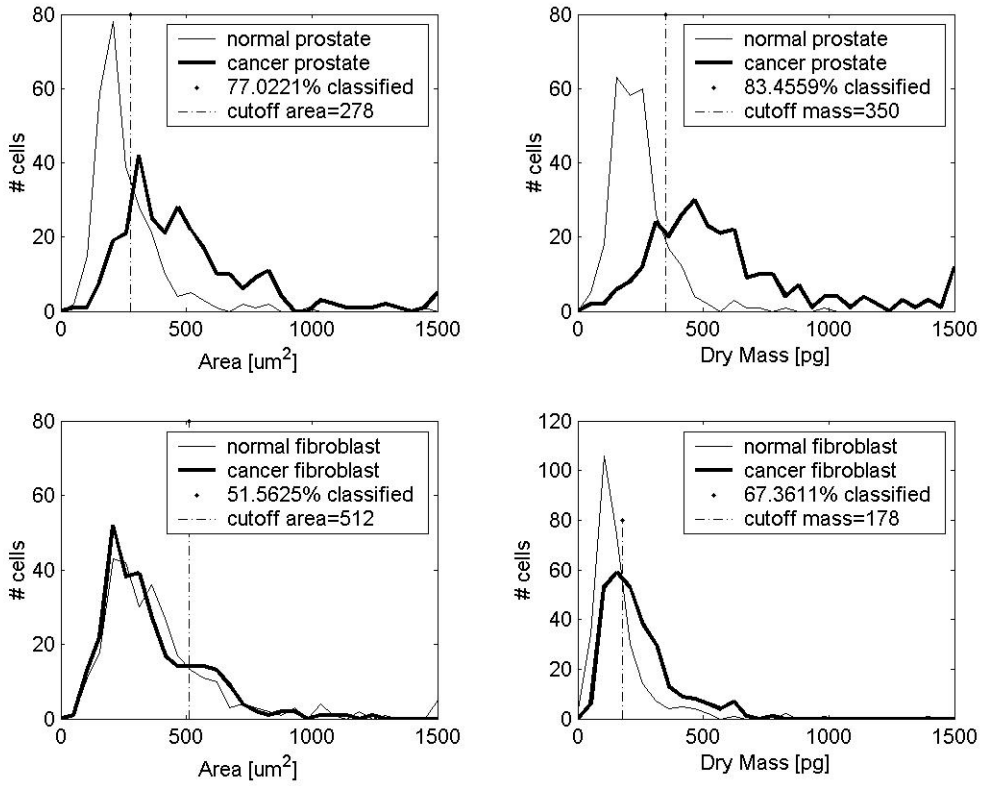

Figure 3.4. Area (left) and mass (right) histograms for normal and cancerous human prostate cells (top) and human fibroblast cells (bottom).

Table 3.1. Population mean and standard deviation

cell type	cell state	# cells	Area (mean± σ) [um^2]	Dry mass (mean± σ) [pg]
prostate	RWPE (normal)	272	255±143	243±121
	PC3 (cancer)	272	502±313	619±469
fibroblast	CCL-171 (normal)	288	414±356	166±139
	CCL-121 (cancer)	288	359±197	239±133

The Lilliefors test rejected the null hypothesis that histogram samples were drawn from populations with normal distributions for all cases. The Wilcox rank-sum test indicated that the normal and cancerous cell histograms of area and mass were identical (5% significance) only for the case of fibroblast cell area (p=0.169). The null hypothesis was rejected for the other three combinations of cell type and parameter. The hypothesis test results and associated p-values are presented in Table 3.2. A test result of 0 indicates acceptance of the null hypothesis, while a test result of 1 indicates hypothesis rejection.

Table 3.2. Wilcox rank-sum test results and associated p-values.

cell type	prostate		fibroblast	
parameter	area	mass	area	mass
test result	1	1	0	1
p-value	<.05	<.05	0.1687	<.05

The effectiveness of using area and mass as parameters to classify normal and cancer cell populations was determined using linear discriminant analysis. Scatter plots presented in Figure 3.5 illustrate the two-dimensional (area and mass) location of samples. By not restricting the decision threshold to one dimension, as in Figure 3.4, the LDA increases classifier accuracy.

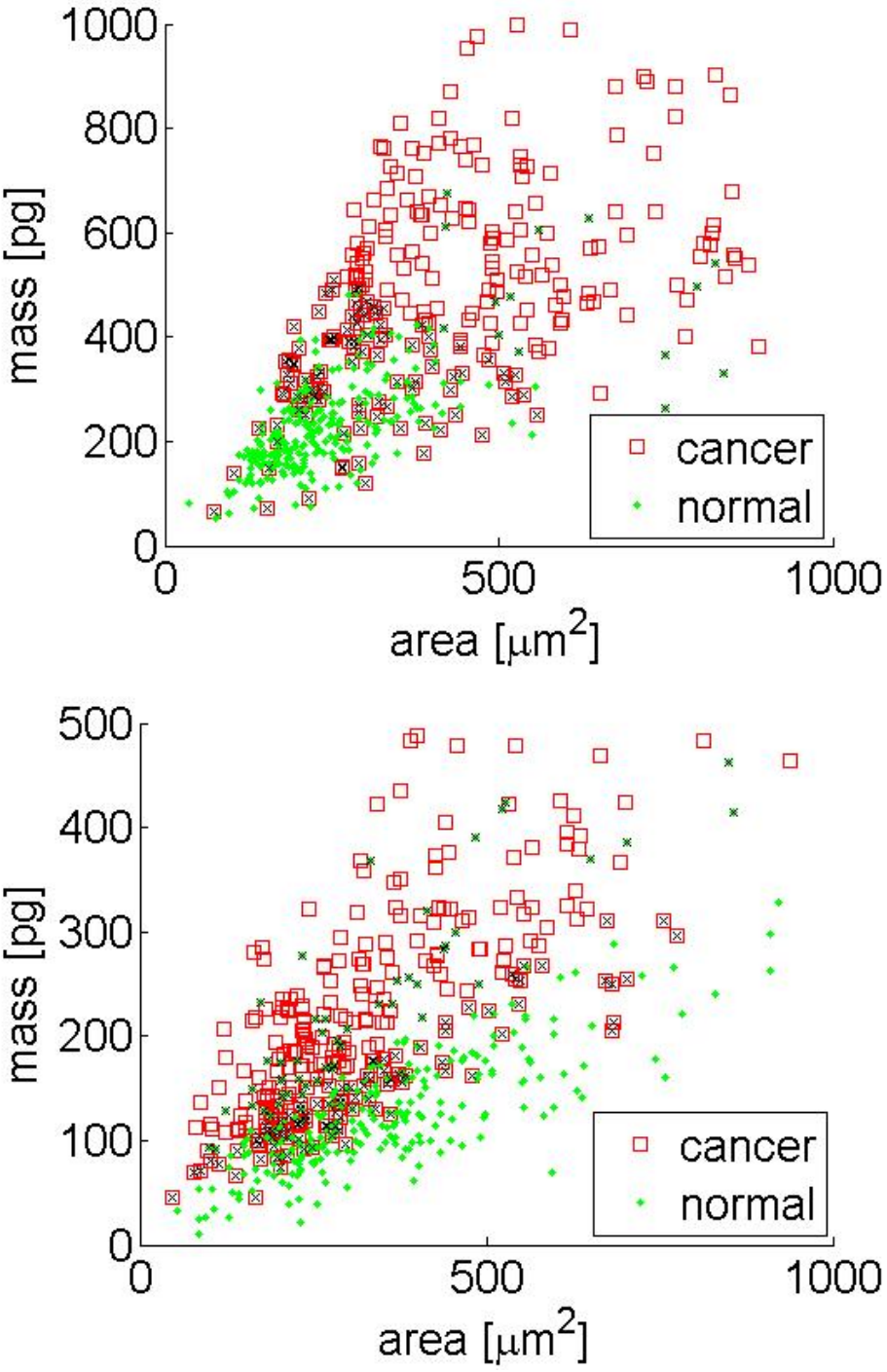

Figure 3.5. Scatter plots (area vs. mass) for: prostate (top) and fibroblast (bottom) samples. X's indicate a misclassified sample.

The LDA achieved a 79% accurate classification rate for the prostate population and a 75% accurate classification rate for the fibroblast population. LDA improved classification accuracy for fibroblast cells compared with classification using only area or mass. LDA improved classification accuracy of prostate cells compared with classification using area only, however, LDA decreased classification accuracy of prostate cells compared with classification using mass only. Using the posterior probabilities returned from the LDA, we calculated the percentage of accurately classified normal and cancer cells for each cell type. See Table 3.3 for classification results.

Table 3. LDA Classification Results

		Prostate	
		Normal	Cancer
%classifed as:	Normal	64.7	6.25
	Cancer	35.3	94.1

		Fibroblast	
		Normal	Cancer
%classifed as:	Normal	67.7	18.4
	Cancer	32.2	81.6

The cross correlation coefficients between area and mass parameters determined for each cell type and state are high (Table 3.4). High correlation is theoretically expected since cell dry mass is a function of area (Equation 3.4).

Table 3.4. Cross correlation Coefficients

cell type	prostate		fibroblast	
cell state	normal	cancer	normal	cancer
cross correlation coefficient	0.739	0.697	0.763	0.779

DISCUSSION

DPC-OCM Advantages/Disadvantages

DPC-OCM is capable of objective, high-resolution quantitative phase imaging. Unlike conventional interference microscopy imaging, in which phase information is coupled into recorded intensity [36-37], DPC-OCM completely decouples amplitude and phase using the Hilbert transform. Another benefit of the DPC-OCM instrument is that the differential phase measurement is made along the axis of the interrogating beam, avoiding the undesirable lateral shear effects common with conventional interference microscopy. Prostate and fibroblast cell dry mass is approximately an order of magnitude greater than epithelial nuclei dry measurements made with interference microscopy [36].

Disadvantages of DPC-OCM include several potential error sources including area and phase measurement error. Calculation of the area of each cell requires identification of the cell boundary by manual or computer automated edge detection. Uncertainty in the cell boundary gives rise to both area and phase error, which propagates into dry mass error. Measurement of cell area requires human or computing time. In certain situations, such as overlapping cells or those only partially within in the field of view, measurement of cell area and mass is compromised. Systematic phase measurement error is possible due to phase wrapping, speckle [43], or sample birefringence. It is unlikely that these potential error sources affected our present experimental results.

Using Dry Mass to Classify Normal/Cancer Cell Populations

Using cell dry mass as and area parameters to discriminate normal and cancerous cell populations results in a 74-79% accurate classification. Dry mass appeared to be a better classifier than area. There are two reasonable explanations for this observation. First, cancer cells are more likely to be larger (volume) than normal cells, and cell mass is dependent on the total volume of the cell. The cell *en face* area is likely to be coupled to volume, but the area-volume dependency is not as strong as the volume-mass dependency. Second, since cancer cells are more metabolically active they have more protein and nucleic acid content per volume (concentration) and hence a higher intrinsic refractive index. Therefore a cancer cell will have greater dry mass than a normal cell of the same volume. This second explanation seems reasonable, but is in disagreement with reference 36. The LDA did not perform drastically better than the classification technique using only one variable, but this is not surprising since cell mass is strongly correlated with cell area.

It is unlikely that area and mass alone are sufficient parameters to discriminate normal and cancerous cells, but nevertheless this data is valuable. The combination of dry mass with additional independent experimental parameters, such as fluorescence labeling, may permit a more effective discriminant analysis. Additionally, if more variables are used, the discriminant score would better fit a normal distribution because of the law of large numbers. The DPC-OCM system may be physically integrated with other diagnostic tools in a single probe capable of multi-modal imaging.

CONCLUSION

DPC-OCM is capable of objective, high-resolution quantitative phase imaging. Potential error sources include area and phase measurement error. DPC-OCM was applied to measure area and dry mass of normal and cancerous cells. Area and mass population averages are greater in the cancerous versus normal state. Using cell dry mass and area as parameters to discriminate normal and cancerous cell populations provides 74-79% accurate classification. Mass is a better classifier than area for both cell types. It is unlikely that area and mass alone are sufficient parameters to discriminate normal and cancerous cells, however, the combination of these with additional independent experimental parameters may prove an effective discriminant analysis tool.

DPC-OCM has the potential to be developed into both an *in vitro* and *in vivo* cell-screening tool. The *in vitro* approach would be similar to the experimental work presented in this paper, in which phase measurement could be performed across a fixed thickness sample chamber. It may be possible to integrate this technique with flow cytometry in order to analyze a large number of cells quickly. The DPC-OCM beam may be scanned in one dimension while cells flow orthogonally across the scan line. One consideration of the process is that cells must be discretely identified.

The greatest potential use of DPC-OCM may be *in vivo* cell-screening. Unlike conventional interference microscopy in which image formation is based on interference of transmitted light, DPC-OCM image formation is based on reflected light. DPC-OCM is a polarization and phase sensitive extension of optical coherence tomography (OCT),

which is a clinically accepted, non-invasive imaging modality. In principle DPC-OCM can provide depth-resolved phase images of *in vivo* cells.

There are, however, great technical challenges facing *in vivo* cell imaging with DPC-OCM. Depth-resolved phase imaging requires an accurate phase measurement at discrete scattering surfaces in the sample. If scattering surfaces are within a coherence length (function of light wavelength and bandwidth) from one another, the interference signal arising from each scattering surface will interfere with each other (speckle). The phase of the recorded fringe signal as well as the position of the scattering surface will be undecipherable due the speckle noise. In order to mitigate this limitiation, greater bandwidth optical sources with greater resolving capabilities may be used.

ACKNOWLEDGEMENTS:

Funding sources include NSF Grant #BES9986296 (Enhancement of Light Propagation in Tissue using Hyper-osmotic Agents) and NSF Grant #DGE9870653 (IGERT Program). The authors also thank Mitchell Kennard who performed the manual edge-detection of the DPC-OCM images.

Chapter 4. Measurement of Chemical Transport Across Individual Cell Membranes Using Optical Path Length Imaging and Modeling

ABSTRACT

We present a novel approach to determine cell membrane transport properties using optical path length (Φ) images acquired with a differential phase contrast optical coherence microscope (DPC-OCM) and a model relating Φ to the forces and flows that characterize the transport process. Experimental dynamic *en face* cell images provide quantitative data from which physical parameters including intra- and extracellular chemical concentration and transient cell volume may be derived. The extracellular chemical concentration stimulus is recorded at the same time and position as the intracellular response of the cell.

An original optical path length model (Φ model) is presented which incorporates coupling across optical, chemical, and osmotic energy domains. The Φ modeling approach possesses several salient features. First, the Φ model is insensitive to the initial and dynamic changes in the shape of the cell, extending validity of experimental Φ data to adherent cells (constant *en face* area) or cells of unknown geometry. Second, the Φ model is capable of simultaneously obtaining the dry mass (protein) of the cell using the

principals of immersion refractometry, obviating the need for independent inactive volume fraction measurement using the Boyle-Van't Hoff technique.

Hydraulic conductivity, Lp (1.33±1.16 μm/(min*atm)), solute permeability, Ps (163±142 μm/min), and inactive volume fraction, Vb (0.13±0.07) were determined for human keratinocytes (n=16) at 25 ^{o}C. The measured values of Lp and Vb are similar to published data measured with other techniques. Potential sources of error in the calculation of membrane transport parameters and advantages of the Φ modeling technique over the conventional approach are discussed.

INTRODUCTION

Accurate measurement of cell membrane transport permeability to water and solutes is important in many fields including cryobiology, pharmacology, tissue engineering, and, recently, tissue optics. The conventional optical technique of determining cell membrane permeability to water and solute is performed by fitting parameters of a theoretical model to experimentally measured *en face* cell area [44]. Requisite inputs to the transport model include initial conditions (all species concentrations and cell volume), an educated initial guess of the cell membrane permeability parameters, and the assumption of a step change in extracellular chemical concentration. The pertinent output generated by the transport model is the change in cell volume. Since only the projected cross-sectional area (*en face*) is measured, a geometrical relationship giving cell volume is necessary. The most accurate membrane permeability parameters (water and solute) are determined by iterating through many possible combinations of these parameters until the error between the theoretical cell area and the experimentally measured dynamic cell area is minimized. Figure 4.1 is a block diagram of the conventional technique of fitting parameters in the transport model.

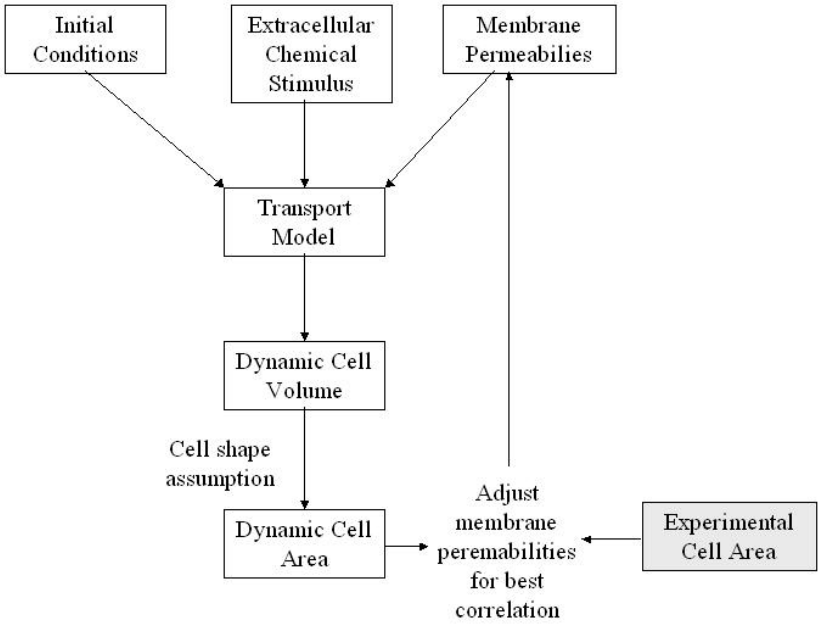

Figure 4.1. Block diagram of conventional technique of fitting transport model cell area to experimentally determined cell area. Legend: White=theoretical model parameters, Shaded=experimental parameters.

Drawbacks of this technique include the need for independent determination of osmotically inactive volume fraction using the Boyle-Van't Hoff technique [45] and the absence of data on the explicit transmembrane concentration difference of the chemical species being transported. Other weaknesses of this technique include the frequently employed assumption of a step change in extracellular solute concentration and the assumption of a pre-defined geometric relationship between cell area and volume (when cell volume is assessed by microscopic observation).

Seminal research regarding "tissue optical clearing" has shown that hyperosmotic agents, including common cryoprotective agents such as glycerol and dimethyl sulfoxide,

cause a transient reduction in tissue turbidity. Proposed mechanisms of this effect include tissue dehydration, refractive index matching between the solute and tissue ground substance, and structural modification at the molecular level [46-48,7]. Optical instrumentation called differential phase contrast optical coherence microscopy (DPC-OCM) [38,39] has been applied to measure changes in refractive index within and surrounding individual cells to better understand quantitatively the optical clearing mechanisms. Refractive index is altered as a direct consequence of the transport of water and solute across cell membranes and thus can be applied as an intrinsic marker useful for bio-transport experiments.

Our research team has demonstrated theoretically and experimentally use of intrinsic refractive index of water and of solute as an indicator of the osmotic driving potential and the molecular flow across individual cell membranes. The combination of experimental Φ images with a model of optical pathlength provides a comprehensive data set from which cell membrane transport parameters can be calculated.

Φ MODEL THEORY

Exposure of a cell to an osmotic agent alters the transmembrane chemical driving potential, resulting in a flux of chemical species across the cell membrane. The flux then alters the chemical composition of the intracellular media and the cell volume. The refractive indices (n) of the intracellular and extracellular compartments are directly dependent on chemical composition. The quantitative spaciotemporal optical pathlength (Φ) of both compartments is a function of their intrinsic refractive index and their extrinsic volume, and therefore Φ can be used as a measure of the transport process.

The optical pathlength measured across a chamber (physical thickness z_2-z_1) containing a cell is the integral product of refractive index and differential thickness (dz) of the chamber (Equation 4.1, Figure 4.2a).

$$\Phi = \int_{z'=z_1}^{z_2} n(z')dz' \tag{4.1}$$

The optical pathlength integrated over a "control area (A_{cv})" (Figure 4.2b) surrounding the cell results in an effective "optical volume." The optical volume divided by A_{cv} defines the spatial average intracellular optical pathlength (Φ_{in}) (Equation 4.2).

$$\Phi_{in} = \frac{1}{A_{cv}} \int_{Acv} \Phi \cdot dA \tag{4.2}$$

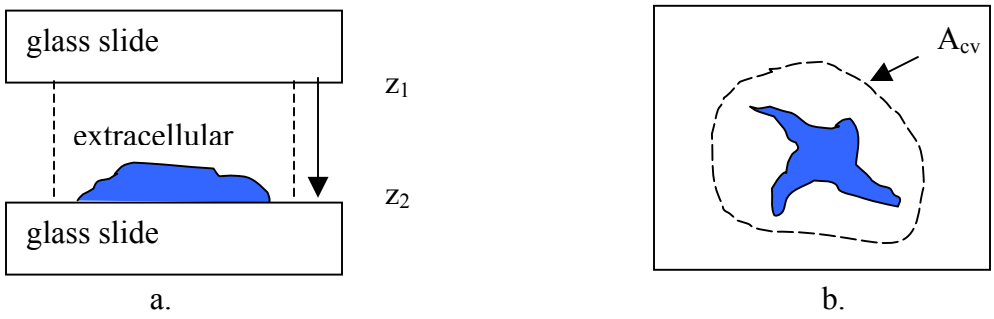

Figure 4.2. a) Side and b) top view of the chamber containing the cell (shaded). The control volume is shown as a dashed line surrounding the cell.

Φ_{in} is dependent on chemical composition and volume of the cell, and independent of cell shape. Unfortunately, it is also dependent on the chemical composition and volume of extracellular medium between the cell boundary and the "control volume" boundary. To alleviate this drawback, the effect of extracellular medium is removed. Differential optical pathlength ($\Delta\Phi$) across the cell membrane is calculated by subtracting the extracellular optical pathlength (Φ_{ex}) from Φ_{in} (Equation 4.3). $\Delta\Phi$ is independent of the shape or absolute volume of the control volume, provided the control volume completely encloses the cell.

$$\Delta\Phi = \Phi_{in} - \Phi_{ex} \tag{4.3}$$

MATERIALS/METHODS

Φ Model Forward Algorithm

The Φ model forward algorithm predicts the ΔΦ cellular response to inputs including the cell membrane water and solute permeabilities, the initial conditions (including all intra- and extracellular concentrations), and the extracellular chemical stimulus. Intermediate calculated variables include dynamic intracellular chemical concentration, from which the intracellular refractive index can be determined, and the dynamic cell volume. This data is used to calculate ΔΦ. The forward Φ model is illustrated in Figure 4.3.

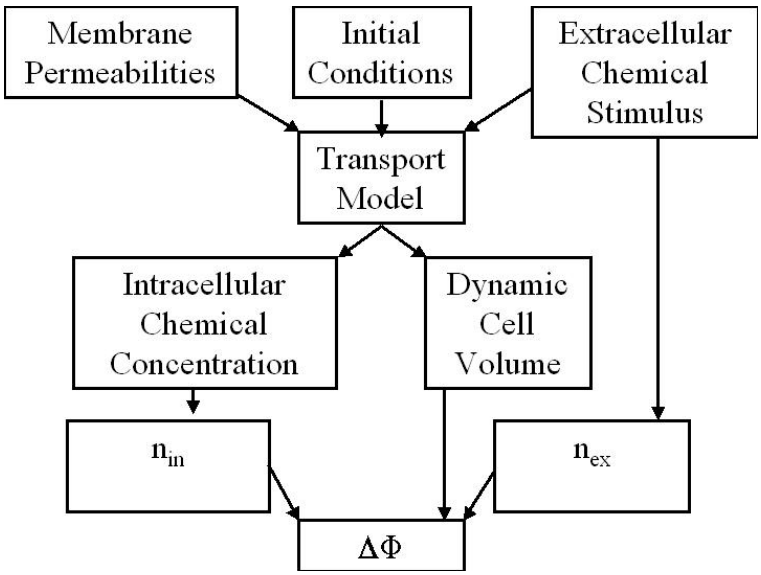

Figure 4.3. Schematic illustration of the forward Φ model.

Several assumptions are built into the forward Φ model. First, the system is composed of four chemical constituents: water, permeable solute, impermeable solute, and protein. Second, the osmotically inactive volume fraction (Vb) is taken as the

volume fraction of protein (Vf_{pro}). Third, the intra- and extracellular environments are well mixed. Fourth, the surface area of the cell available for transport equals the initial surface area of the cell. The model assumes the cell membrane is selectively permeable to water and permeable solute, but impermeable to protein and impermeable solute. Assuming no interaction between the transport of water and permeable solute, the Kedem-Katchalsky transport equations [44] reduce to:

$$\frac{dV_w}{dt} = -Lp \cdot A \cdot R \cdot T \cdot (M^e - M^i) \tag{4.4}$$

$$\frac{dN_{per}}{dt} = Ps \cdot A \cdot (M^e_{per} - M^i_{per}) \tag{4.5}$$

Important parameters, their description, values, and units are summarized in the Appendix. Since the chamber volume and control volume are conserved, the volume of water and permeable agent that diffuse out of the cell equals the volume of extracellular fluid added above or adjacent to the cell.

The constitutive laws governing this system include the constant refractive index (n_s) and the constant molar volume (V_s) of each pure substance (s). Refractive index (n) of a mixture is given by the Clausius-Masotti equation [49]:

$$3\left(\frac{n^2 - 1}{n^2 + 2}\right) = \sum_s N_s \alpha_s \tag{4.6}$$

where N_s is the number density of atoms of each chemical constituent and α_s is the constant polarizability of each constituent.

Solution of the model requires several input parameters including the initial intracellular and extracellular chemical concentrations, which may be calculated using

the following constraints. The cell is initially isoosmotic with its extracellular environment and initially contains no permeable solute. Also, the sum of volume fractions of all four chemical species is unity.

Φ Model Inverse Algorithm

Experimental data and the Φ model inverse algorithm provides a method to estimate membrane permeability parameters (Lp and Ps) and osmotically inactive volume fraction (Vb). The inverse solution utilizes the relationships governing chemical concentration and refractive index described in the forward Φ model. Three experimentally measurable parameters ($\Phi_{in}(t)$, $\Phi_{ex}(t)$, and $\Delta\Phi(x,y,t=0)$) are input into the Φ model. The Levenberg-Marquart optimization algorithm iterates through many possible combinations of Lp, Ps, and Vb until the theoretical ΔΦ provides the best correlation with the measured ΔΦ. The directed iteration process attempts to minimize the sum-of-squared error between theoretical and measured ΔΦ. Figure 4.4 is a block diagram of the Φ inverse model.

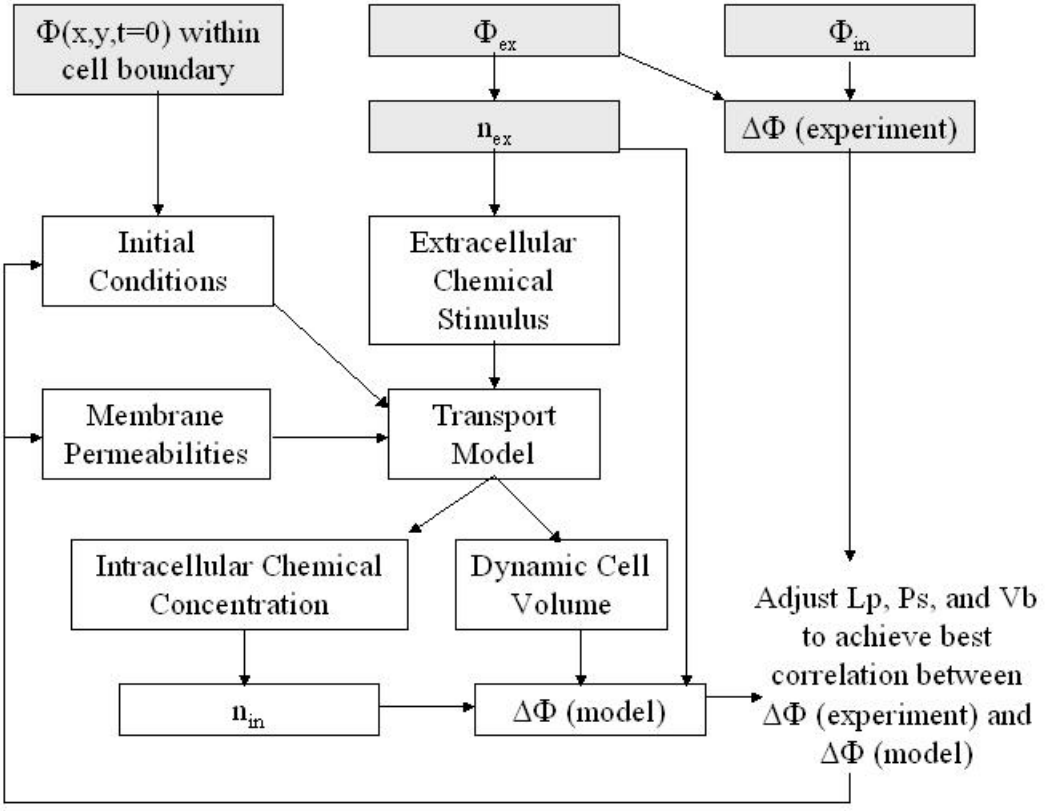

Figure 4.4. Schematic illustration of the inverse Φ model. Legend: White=theoretical model parameters, Shaded=experimental parameters.

Immersion refractometry may be used to measure individual cell dry mass or Vb [18]. Conventionally, this technique uses two differential optical path length measurements: ΔΦ when the cell is immersed in a low refractive index liquid (like water) and likewise when the cell is immersed in a high refractive index nonpermeable liquid (like albumin). The principals of this technique remain valid using a high refractive index permeable liquid if the extracellular perfusion and the transport of water and

permeable solute are properly accounted for. Vb is calculated inversely along with Lp and Ps since they are all coupled to ΔΦ.

The surface area of the cell may be calculated based on Vb and the initial spatial distribution of Φ within the cell boundary, assuming protein is well mixed within the cell.

Φ Imaging Using DPC-OCM

DPC-OCM directly measures a differential phase change which may be converted to relative optical pathlength at a given lateral position and time [33,34,38,50]. The sample path optics are configured for the specific cell sample preparation as shown in Figure 4.5. Cells are cultured on a glass slide, a latex gasket is applied, and a second glass slide (with perfusion inlet and exit ports) is positioned above the gasket. Two clamps apply pressure to the glass slides creating a constant chamber thickness. Four birefringent prisms are used to induce a relative path-length delay between the two orthogonal polarization channels. In this manner, the Ch2 interferogram produced by the glass interface above the cell is temporally retarded (axially separated) to occur simultaneously with the Ch1 interferogram produced by the glass interface below the cell. The Ch2 interferogram acts as a reference while the Ch1 interferogram passes through the cellular sample and extracellular medium, acquiring relevant specimen information. The two coaxial channels (no lateral separation) are reflected from scanning mirrors and directed through a high-numerical-aperature (N.A.=1.4) 40X microscope objective, producing a 3 μm FWHM beam diameter in the focal plane. The focal plane corresponds with the center of the chamber.

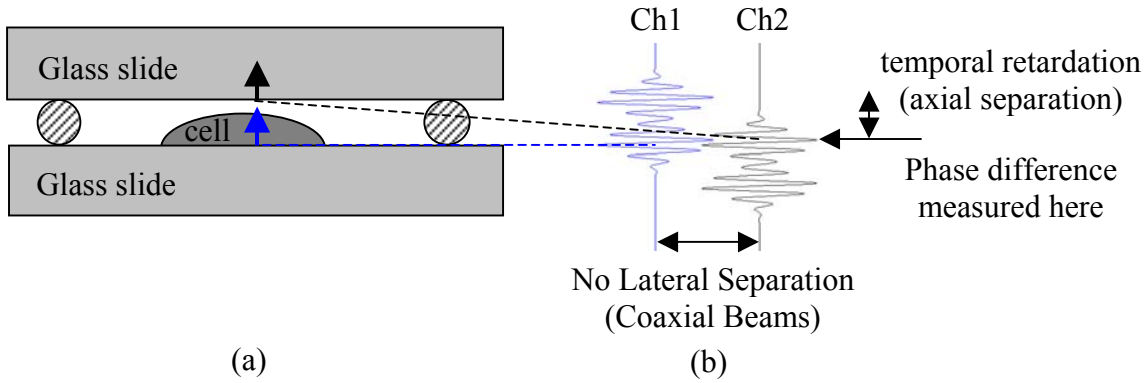

Figure 4.5. (a) Side-view schematic representation of sample preparation. Arrows represent backreflected light which interferes simultaneously. (b) A-scans reveal the light amplitude reflected from the two glass slides and thus provide feedback for focusing and adjusting the temporal delay (axial separation) between the two channels.

Phase difference between the two channels, $\Delta\phi=\phi_2-\phi_1$, rejects common-mode phase noise present in both channels. The optical path length relative to its initial value ($\Phi-\Phi_o$) can be calculated from the phase difference with 1 nm resolution by:

$$\Phi - \Phi_o = \frac{(\Delta\phi - \Delta\phi_o)\lambda_c}{4\pi} \tag{4.7}$$

The DPC-OCM system has a fixed optical integration time which creates a tradeoff between the temporal resolution, spatial resolution, field of view, and acquired data file size. Currently 0.25 s is required to scan a 80x90 μm^2 area with 3 μm lateral resolution, 10 KHz carrier fringe frequency, and 100 KHz sampling frequency. A 15 s scan requires approximately 6 MB of binary data, which must be saved to RAM during acquisition. Increasing scanning speed is desirable for observation of the chemical

transport event, but requires increased fringe and sampling frequency (and file size) to preserve the integrity of the recorded phase data.

Cell Sample Preparation and Perfusion

Adherent human keratinocytes HPV16 E6/E7 (ATCC# CRL-2309) were cultured on glass optical flats according to ATCC protocol [51]. Glass coverslips were sterilized in alcohol and coated with poly-l-lysine to allow cell adhesion. The cells were grown in keratinocyte-serum free medium (Gibco 17005-042) supplemented with 0.05 mg/ml bovine pituitary extract and 35 ng/ml epidermal growth factor. Cells were incubated at 37 ^{o}C with a 5% CO_2 in air atmosphere. Two subculture procedures (two passages) were performed prior to experimentation.

Individual optical flats and adherent cells were rinsed with isotonic saline solution to remove debris immediately prior to experimentation. The cell perfusion chamber was assembled as described previously, and perfusate inlet and exit ports were connected to their corresponding reservoirs using a 1 mm inner diameter plastic tube. Isotonic saline solution was administered into the chamber for 60 s to remove debris and purge air bubbles. A 20% by volume glycerol solution (2.8M) was administered into the sample chamber immediately following saline perfusion via a manual valve. Perfusion driving force was supplied using a gravity pump (approx 1 ft static pressure head). *En face* DPC-OCM video images directly quantify Φ in two spatial dimensions (80x90 μm^2) and time (15 s).

Image Processing

The A_{cv} boundary was set by manual tracing around the edge of the cell. Φ_{ex} was calculated using a three-step process. First, $\Phi(x,y,t)$ was cropped within A_{cv}. Next, a new $\Phi(x,y,t)$ within A_{cv} was estimated using spline-interpolation of A_{cv} boundary values. The Matlab griddata function uses Delaunay triangulation to linearly interpolate interior values, and the interpolated surface always goes through the A_{cv} boundary. Φ_{ex} was calculated by averaging the new interpolated $\Phi(x,y,t)$ within A_{cv} in the same manner that Φ_{in} is calculated.

Cell surface area is calculated using the three-dimensional cell profile. First, median spatial filtering is applied to smooth the initial Φ image. Based on the value of Vb and the filtered Φ image, cell height is determined for all lateral positions within the A_{cv} boundary. Only values of cell height greater than a threshold amount (1 μm) and contained within A_{cv} were considered valid. The gradient of the spatial distributions of cell height was calculated in the x- and y- lateral dimensions. The cell surface area was calculated based on cell height and the height gradient (cell slope).

RESULTS

Φ Model Simulations

To illustrate utility of the Φ modeling technique several simulations were performed using parameter values given in Appendix A. Variables used in the simulations include the water and solute permeabilities (Lp=0.1 and 1, and Ps=10 and 100), and osmotically inactive protein volume fraction (Vb=0.1 and 0.3). The surface area to volume ratio of the cell was 0.6 μm^{-1}. The ranges of selected values were based on typical values published for other cell types and solutes [14-15]. Φ_{ex} experimental data was used as the input osmotic stimulus for the simulations (Figure 4.6).

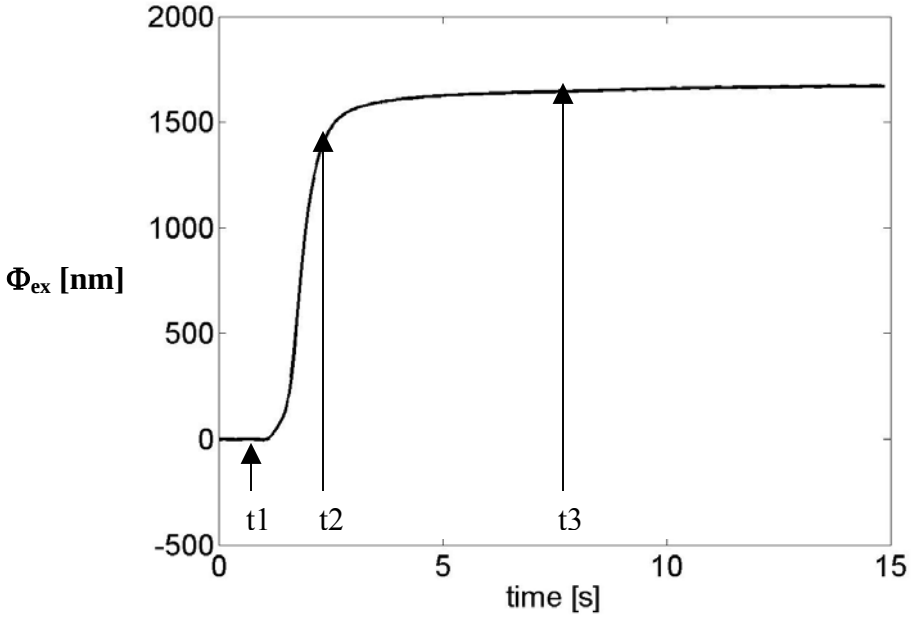

Figure 4.6. Φ_{ex} vs time. The three markers, t1-t3, indicate times corresponding to: t1 initial state, t2 immediately after perfusion with glycerol, t3 equilibrium after perfusion with glycerol.

The simulated ΔΦ response of the cell (Figure 4.7) is normalized by dividing by its initial value and therefore independent of absolute cell volume. Initially (t1) ΔΦ is positive because the isoosmotic cells contain high refractive index protein. Immediately after perfusion with glycerol (t2) ΔΦ is reduced and can even become negative since the refractive index of water within the cell is much less than the high refractive index of extracellular glycerol. When the cell reaches an equilibrium state after perfusion with glycerol (t3) the intracellular and extracellular concentrations are again isoosmotic. The reason ΔΦ does not return to its initial value is because refractive index of isoosmotic fluid (n=1.4) is closer to refractive index of osmotically inactive protein (n=1.54). The value ΔΦ approaches at t3 (86%) is defined by the ratio of differential refractive index between protein and isotonic fluid in the perfused and initial states (equation 4.8).

$$\frac{n_{pro} - n_f^p}{n_{pro} - n_f^i} = \frac{1.54 - 1.36}{1.54 - 1.33} = 0.86 \qquad (4.8)$$

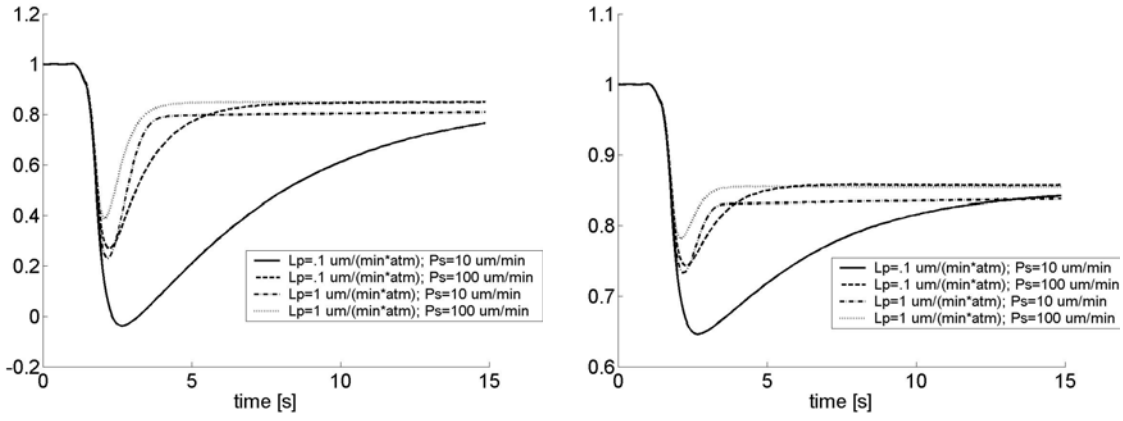

Figure 4.7. Simulated ΔΦ response (normalized) as a function of input variables Lp, Ps, and Vb. Vb=0.1 (left) and Vb=0.3 (right).

Φ Model Inverse Solution Using Experimental Data

DPC-OCM was successfully employed to observe transmembrane chemical transport resulting from application of a 20% by volume glycerol solution to adherent human keratinocytes. *En face* video images directly quantify Φ(x,y,t) as depicted in Figure 4.8. These images were analyzed to obtain the ΔΦ excursion which is presented in Figure 4.9.

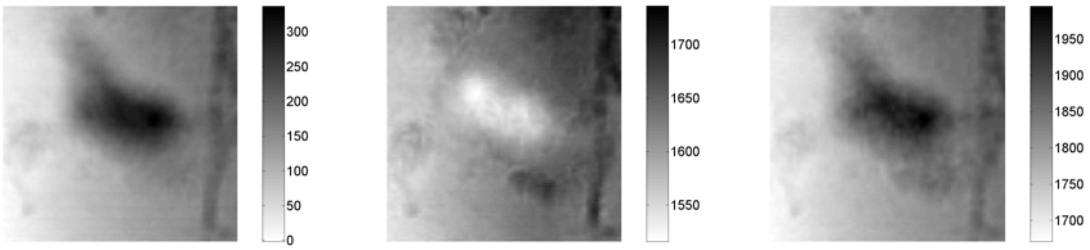

t1 t2 t3

Figure 4.8. Φ images [nm] vs. time (t1-t3) corresponding with the markers in Figure 4.6. Field of view is 80x90 μm^2.

The inverse Φ model was fit to the ΔΦ experimental data as illustrated in Figure 9, yielding values for the membrane permeability parameters and the volume fraction of protein. Hydraulic conductivity, Lp (1.33±1.16 μm/(min*atm)), solute permeability, Ps (163±142 μm/min), and inactive volume fraction, Vb (0.13±0.07) were determined for human keratinocytes (n=16) at 25 ^{o}C. A summary of individual results is presented in Table 4.1. Initial guesses for Lp, Ps, and Vb were 1 μm/(min*atm), 100 μm/min, and 0.2, respectively. For all analyses, the Levenberg-Marquart optimization algorithm converged on a solution prior to 100 iterations.

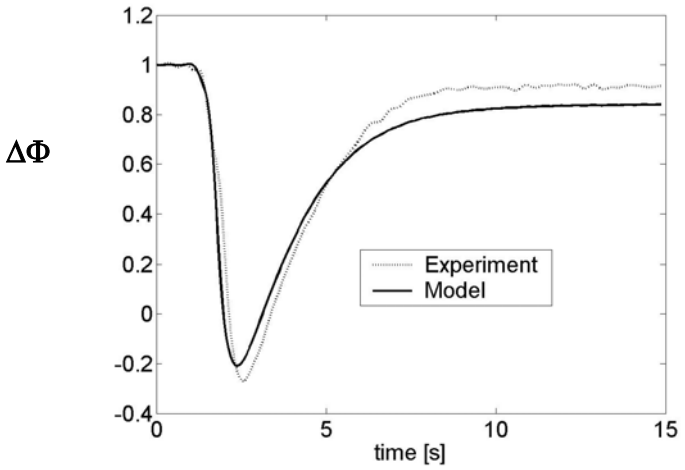

Figure 4.9. ΔΦ (normalized) experimental data and best-fit model data.

Table 4.1. Experimental Results and Published Parameter Values

Sample number:	Lp	Ps	Vb	surface area	initial volume	SA/volume
	[um/min/atm]	[um/min]		[um^2]	[um^3]	[1/um]
1	0.75	155	0.10	3633	8648	0.42
2	2.23	506	0.13	825	2550	0.32
3	0.99	92	0.22	720	1106	0.65
4	1.32	113	0.12	1547	4168	0.37
5	1.20	188	0.07	2260	7543	0.30
6	3.82	449	0.11	3322	13253	0.25
7	0.72	13	0.09	846	2731	0.31
8	2.59	133	0.05	3385	12896	0.26
9	2.56	49	0.16	905	2687	0.34
10	2.87	266	0.07	1754	6666	0.26
11	0.01	59	0.27	173	373	0.46
12	0.07	103	0.19	355	711	0.50
13	0.61	53	0.07	2488	8776	0.28
14	0.01	56	0.17	846	1928	0.44
15	0.20	115	0.25	209	711	0.29
16	1.31	261	0.08	2487	7019	0.35
mean	1.33	163	0.13	1610	5110	0.36
standard deviation	1.16	142	0.07	1179	4252	0.11
Published Values:						reference
human keratinocyte	0.19		0.17			[52]
hamster fibroblast	0.70					[53]
human chondrocyte		0.92				[54]
human spermatozoa		15.4				[55]

DISCUSSION

The large standard deviation of our experimentally measured parameter values may be attributed to variability in keratinocyte maturation. As keratinocytes mature, they undergo the process of cornification. Highly cornified keratinocytes, called corneocytes, compose the outer layer of the epidermis, the stratum corneum. The stratum corneum provides the barrier function of skin, and as such has a very low water and solute permeability compared with deeper skin layers. Published values of Vb=0.17 and Lp=0.0375 μm/(min*atm) are reported for human keratinocytes at 0 ^{o}C [52]. Extrapolation with the Arrhenius relationship gives Lp=0.19 μm/(min*atm) at 25 ^{o}C. Chinese hamster fibroblasts in the presence of 0.5 M glycerol were reported to have Lp=0.70 μm/(min*atm) at 25 ^{o}C [53]. Glycerol permeability of human chondrocytes is Ps=0.92 μm/min [54], while that of human spermatozoa is Ps=15.4 μm/min [55].

The conventional method of determining cell membrane permeability parameters utilizes only one experimentally measured parameter, namely *en face* cell area, and the assumption of constant cell shape (usually spherical). This technique works well if the assumption of cell shape is accurate, and therefore spherically shaped cells in suspension are often used. Several drawbacks are recognized when using non-adherent cell specimens for cell membrane transport experiments. First, cell membrane transport properties of adherent and suspended cells may differ. Adherent cell properties are though to better represent *in vivo* properties. Second, the extracellular perfusate flow rate must be limited to prevent washing away of cells, prohibiting the desirable administration of a step change in extracellular solution concentration.

Several benefits are evident when comparing the Φ method over the conventional method. Most importantly, the Φ method utilizes three independent experimentally measured parameters (Φ_{in}, and Φ_{ex}, and $\Phi(x,y,t=0)$ within the cell boundary) resulting from both the chemical driving force and flow responsible for the dynamic event. The Φ method works for unknown or irregularly shaped cells since no relationship between cell *en face* area and volume is required. The initial cell surface area may be calculated using the initial Φ spatial distribution. The extracellular solution concentration in direct contact with an individual cell can be explicitly measured and therefore the conventional assumption of a step change in concentration is not required. Also inconsequential is if the transport of intracellular water or solute out of the cell effects the extracellular environment. The Φ model is capable of simultaneously obtaining the dry mass (protein) and Vb of the cell using the principals of immersion refractometry, obviating the need for independent inactive volume fraction measurement using the Boyle-Van't Hoff technique. Experimental data may potentially be processed more accurately and quickly since no automated or manual edge detection of the cell is required (provided no portion of the dynamic area of the cell ever extends beyond the control volume).

Optimal conditions for observing a large Φ excursion includes cells that lose a large amount of water in response to the transport process. The Φ excursion is also greater when the permeable solute has a very different refractive index than water (n=1.33). This condition is true for many hyperosmotic agents of interest such as glycerol (n=1.47), dimethyl-sulfoxide (n=1.45), and polyethylene glycol (n=1.46). High

concentrations of permeable and/or impermeable solute increase the dynamic range of Φ, which is proportional to refractive index and therefore to solute concentration.

Experimental data and the theoretical model did not correspond well for all samples in the equilibrium state after perfusion with glycerol (e.g. Figure 4.9). This result is likely due to error in the Φ analysis technique which may arise due to the assumption that the protein volume fraction is osmotically inactive. A portion of the protein may be osmotically active, and a better fit of the model to experimental data is possible if properly accounted for.

Several fundamental experimental error sources may adversely affect quantitative Φ images, depending on conditions of the DPC-OCM system and the cellular sample. The data and results presented in this paper are believed to be unaffected by these types of fundamental error since the conditions for causing error were not present, nor were characteristic signs of error. Nevertheless, it is useful to illustrate potential error sources and their characteristic signs. In additional experiments not presented in this paper, cells were reperfused with saline following loading with glycerol, and we believe these fundamental error sources adversely affected measured Φ images.

One fundamental error source is "speckle" [43] caused by interference of discrete scatterers separated by less than a coherence length (~25 μm). If an undesirable interference signal is produced within or at the top surface of the cell, this interferogram may interfere with one or both of the signal channels (Ch1 or Ch2, figure 4.6). This potential error source may be eliminated by mechanically isolating the signal channels from reflections that may originate from within the cell.

Another fundamental error source is phase averaging over the finite width of the interrogating optical beam. This effect introduces a greater artifact if the cell has steep-sloping sides and/or large intracellular refractive index. If the sample induces a phase field over the beam spot with values ranging greater than 2π, the detected phase will be an average of the 2π modulus of the actual phase field (Figure 4.10). This potential artifact may be reduced by decreasing the beam diameter.

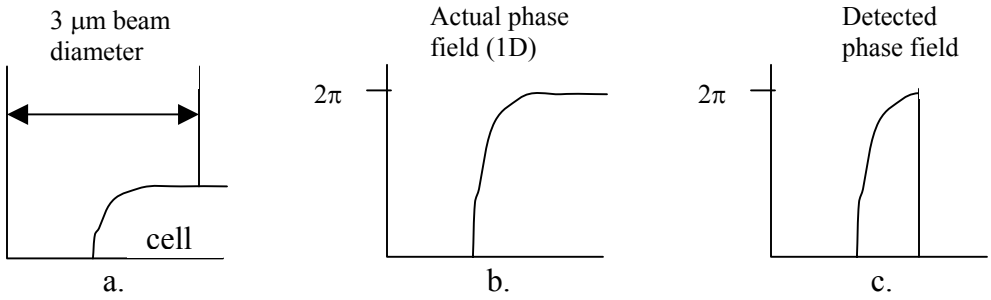

Figure 4.10. Relationship between actual phase field (b) induced by a sample (a) and the detected phase value at one position of the beam (c).

A third possible fundamental error source is caused by an insufficiently fast fringe modulation frequency relative to the speed of the laterally scanning galvos. Approximately one fringe (2π radians) should be generated before the beam is laterally scanned by one beam diameter. This potential error source may be eliminated by either slowing the lateral scan speed or increasing the fringe modulation frequency. The tradeoff of decreasing the lateral scan speed is that the dynamic transport event may be undersampled. The tradeoff of increasing the fringe modulation frequency is that the sample frequency, and therefore data file size will also necessarily increase.

A fourth fundamental error source may arise if the cellular sample is birefringent, nonuniformly retarding the polarized light passing through the cell at different spatial locations. This is a fundamental limitation of a polarization sensitive DPC-OCM and cannot be eliminated in the current implementation.

CONCLUSION

A Φ model was engineered relating optical path length to the transport of chemical species across cell membranes. DPC-OCM was utilized to acquire experimental Φ video images during osmotic challenges of 16 human keratinocytes at 25 ^{o}C. Lp (1.33±1.16 μm/(min*atm)), solute permeability, Ps (163±142 μm/min), and inactive volume fraction, Vb (0.13±0.07) were determined using the experimentally acquired Φ images and the inverse Φ transport model.

The Φ experimental/modeling technique possesses several salient features over the conventional transport modeling technique. First, the Φ method works for unknown or irregularly shaped cells. Second, the Φ model is capable of simultaneously obtaining the dry mass (protein) of the cell using the principals of immersion refractometry, obviating the need for independent inactive volume fraction measurement using the Boyle-Van't Hoff technique. Third, the extracellular solution concentration in direct contact with an individual cell can be explicitly measured and therefore the conventional assumption of a step change in concentration is not required.

Potential error sources in both the experimental and model components of the transport parameter estimation technique have been identified. Future improvements should yield more consistent and accurate values of water and solute permeabilities and protein volume fraction since the likely error sources do not appear to be fundamental limitations.

ACKNOWLEDGEMENTS

Funding sources include NSF Grant #BES9986296 (Enhancement of Light Propagation in Tissue using Hyper-osmotic Agents) and NSF Grant #DGE9870653 (IGERT Program). The authors also thank Mitchell Kennard who performed the manual edge-detection of the DPC-OCM images.

Chapter 5. Dehydration Mechanism of Optical Clearing in Biological Tissue

ABSTRACT

Dehydration induced by evaporation or osmotic stimuli such as hyperosmotic chemical agents appears to be a primary mechanism of optical clearing in collagenous and cellular tissue. OCT and photographic images indicate that air-dried skin and tendon samples are as transparent as hyperosmotic agent treated samples. In addition, skin immersed in high refractive index DMSO does not optically clear as predicted by the hypothesized refractive index matching mechanism. TEM images reveal that dehydration causes individual scatterers (collagen fibrils and organelles) to become more closely packed, but does not cause a noticeable change in scatterer size. Rayleigh-Gans theory predicts this ultrastructural change contributes substantially to optical clearing.

INTRODUCTION

Tissue Optical Clearing

The response of tissue to hyper-osmotic agents is a reduction in light scattering and corresponding increase in optical clarity. "Tissue optical clearing" permits delivery of near-collimated light deeper into tissue potentially improving the capabilities of optical diagnostic and therapeutic applications.

Numerous scientific publications discuss advantages and methods of tissue optical clearing using hyper-osmotic agents [1-3], yet understanding of the mechanisms of clearing remains incomplete. Three hypothesized mechanisms of light scattering reduction induced by hyper-osmotic agents include: 1) dehydration of tissue constituents [1,2], 2) replacement of water (interstitial or intracellular) with an agent that better matches the higher refractive index (n) of the proteinaceous structures [1,2], and, 3) structural modification or dissociation of collagen [7]. The refractive index matching mechanism (#2) requires dehydration (#1), but is unique due to its additional feature: repacement of water with agent. These and other unknown dynamic mechanisms may be working synergistically or antagonistically with different relative contributions. Additionally, each hyperosmotic agent may optically clear tissue by some unique combination of mechanisms.

The three hypothesized tissue clearing mechanisms result from the transient transport of water and/or hyper-osmotic agents in response to chemical concentration gradients. Hyperosmotic agents alter the scattering properties of tissue through changes to: 1) scatterer refractive index, 2) scatterer bathing media refractive index, 3) scatterer

size, 4) scatterer shape, and 5) scatterer packing density (volume fraction, ϕ). All parameters experience a controlled transient excursion dependent on the tissue (cells and/or collagen) permeability to water and hyperosmotic solute [11-14]. This paper explores in detail the effects of tissue dehydration on scatterer bathing media refractive index and scatterer packing density.

The purpose of this paper is twofold: 1) to provide evidence supporting our claim that tissue dehydration is a primary mechanism of tissue optical clearing, and 2) to explain how this mechanism functions to reduce scattering. The first aim will be accomplished by measuring optical scattering changes between native and dehydrated tissue states using optical coherence tomography (OCT) and transmission/reflection photography. Specifically, we will compare tissue clearing efficacy between hyperosmotic agent induced dehydration (which also causes refractive index matching) and evaporative dehydration (which isolates this mechanism of clearing). The second aim will be accomplished in two parts. First, changes in tissue ultrastructure due to dehydration are determined using transmission electron microscopy (TEM) and simulated using a cell membrane transport model. Second, Rayleigh-Gans modeling is used to simulate light scattering effects due to tissue refractive index and ultrastructural changes.

Origins of Light Scattering in Tissue

To understand the mechanisms of reduced scattering following application of a hyperosmotic solute, the origins of tissue scattering must first be known. Scattering results from the interaction of light with the nonisotropic refractive index of a material.

The spatial refractive index distribution of a material specifies the magnitude and direction of scattered light of a given wavelength. Although Mie theory has successfully predicted scattering properties of cells and other scatterers in living tissue [22,56-58], the theory is only applicable to spheres.

The Rayleigh-Gans approximation to Mie theory is suitable for arbitrarily shaped particles that have a size comparable to the wavelength of the scattered light [59,60]. The Rayleigh-Gans equation (Equation 5.1) expresses reduced scattering cross section (σ_s' [cm^2]) as a function of scattering particle radius (r), scattering particle refractive index (n_{in}), surrounding medium refractive index (n_{ex}), and wavelength of light in vacuum (λ):

$$\sigma_s' = \frac{9}{256\pi}\left|\frac{m^2-1}{m^2+2}\right|^2\left(\frac{\lambda}{n_{ex}}\right)\int_{\theta=0}^{\pi}\left(\left(\sin(u)-u\cos(u)\right)^2\frac{\left(1+\cos^2\theta\right)\sin\theta\left(1-\cos\theta\right)}{\sin^6\left(\frac{\theta}{2}\right)}\right)d\theta \quad (5.1)$$

where $m=\frac{n_{in}}{n_{ex}}$, $u=2\cdot\frac{2\pi r n_{ex}}{\lambda}\cdot\sin\left(\frac{\theta}{2}\right)$, and θ is scattering angle.

For materials such as tissue composed of densely packed scatters (volume fraction, ϕ>0.5) the reduced scattering coefficient (μ_s' [cm^{-1}]) is related to the reduced scattering cross section by [58,61]:

$$\mu_s' = \frac{3\phi(1-\phi)}{4\pi r^3}\sigma_s' \quad (5.2)$$

The quadratic relationship between ϕ and reduced scattering coefficient is plotted in Figure 5.1. From this relationship, it is obvious that maximum scattering occurs for a scatterer volume fraction equal to 0.5.

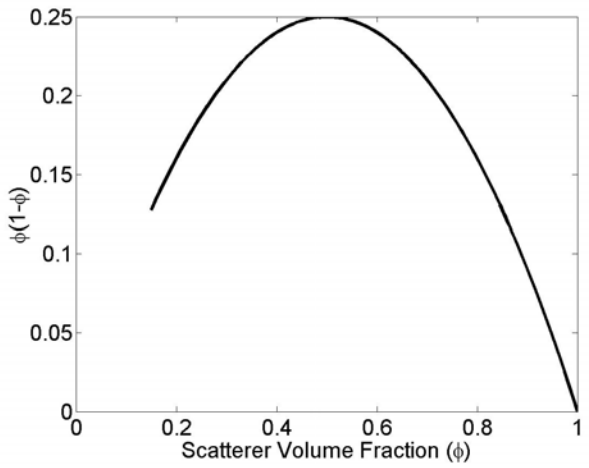

Figure 5.1. Relationship between reduced scattering coefficient, μ_s', and scatterer volume fraction, ϕ.

Equations 1 and 2 are used to simulate reduced scattering coefficient as a function of scatterer radius ($0<r<1$ μm) at two different wavelengths (Figure 5.2). The wavelengths chosen for this analysis represent diagnostically [fluorescence microscopy (0.5 μm) and OCT (1.3 μm)] and therapeutically relevant wavelengths. The reduced scattering coefficient is assumed independent of the absorption coefficient (which is much smaller than the scattering coefficient at these wavelengths). Reasonable values of refractive index ratio m=1.05 [58] and volume fraction ϕ=0.5 [62] are used for this simulation. For the wavelengths considered, reduced scattering coefficient is maximum for particles with a radius of about $\lambda/5$. Scattering decreases sharply for smaller scatterer

radii, and decreases more gradually for larger radii. Results computed from other light scattering models such as the finite difference time domain (FDTD) method [63,64] are consistent with these observations.

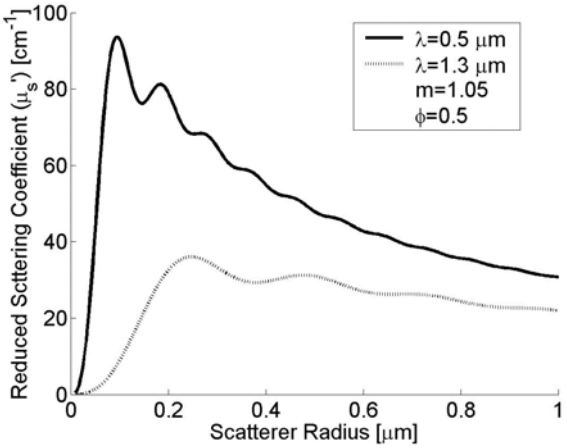

Figure 5.2. Reduced scattering coefficient vs. scatterer radius for a visible and a near-IR wavelength.

Biological tissue consists of cells and collagen and contains numerous highly scattering sub-micron sized scatterers. Furthermore, these sub-micron sized scatterers occupy a large volume fraction of the tissue (ϕ=0.2-0.5). For example, consider the organelles constituting a typical hepatocyte as shown in the TEM image of Figure 5.3 [62]. All of the intracellular organelles (with the exception of the nucleus) have a radius less than 0.5 μm. The percent volume fraction and radius of the main intracellular organelles are listed in Table 5.1. The radius is listed only for organelles with an approximately spherical shape.

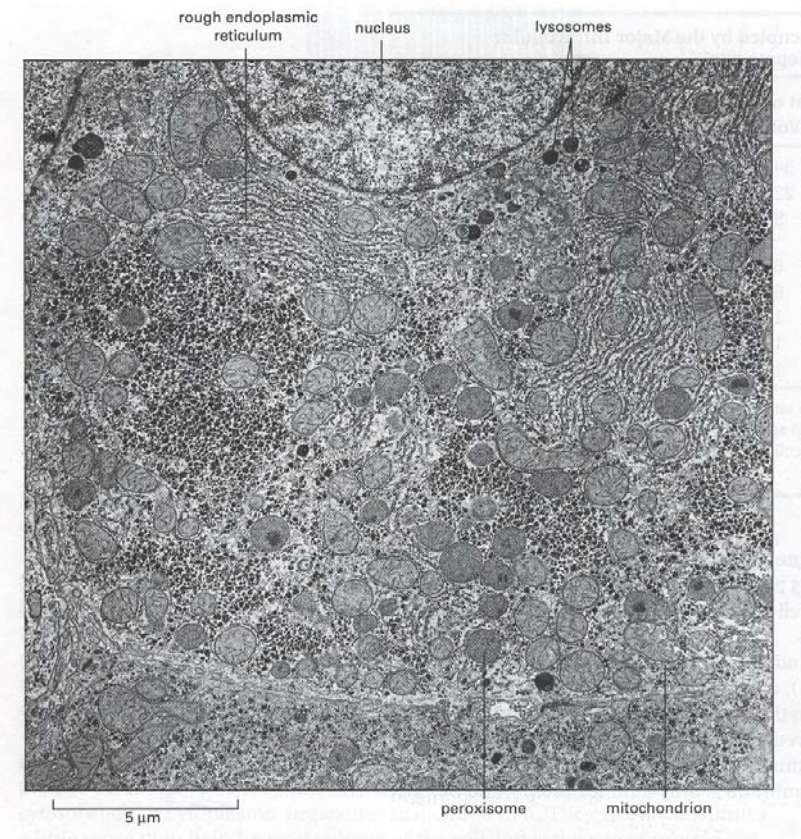

Figure 5.3. Electron micrograph of part of a hepatocyte seen in cross section. Several intracellular organelles are indicated [62].

Table 5.1. Hepatocyte organelle size and volume fraction [62]

Intracellular Compartment	Percent of total cell volume	Approximate number per cell	Approximate radius (um)
Cytosol	54	-	-
Mitochondria	22	1700	0.5
Rough ER cisternae	9	-	-
Smooth ER cisternae plus Golgi cisternae	6	-	-
Nucleus	6	1	4.2
Peroxisomes	1	400	0.3
Lysosomes	1	300	0.3
Endosomes	1	200	0.4

MATERIALS AND METHODS

Optical Clearing Experiment

The first aim of this paper is supporting our hypothesis that dehydration is a primary mechanism of optical clearing with hyperosmotic agents. Evidence to support this claim includes OCT and photographic images which provide a quantitative measure of light scattering from tissue dehydrated by: 1) evaporation (no application of agents), and 2) application of hyperosmotic agents including glycerol and dimethyl sulfoxide (DMSO). Evaporation isolates the dehydration mechanism of optical clearing from the other proposed mechanisms (i.e., refractive index matching by agents or structural modification of collagen). If evaporation is as successful at reducing light scattering as the hyperosmotic agents, then dehydration may be the dominant mechanism of tissue optical clearing.

We must emphasize, however, that refractive index-matching may occur as a consequence of the mechanism of dehydration, and the two cannot be physically uncoupled. As water is removed from tissue, proteoglycans and suspended proteins become more concentrated and refractive index of the interstitial or intracellular fluid increases and more closely matches that of the proteinaceous structure (e.g. collagen, membranes). This type of refractive index matching is due to native agents and a passive process, and we wish to discern it from index matching due to foreign hyperosmotic agents intentionally introduced to the tissue.

Tissue samples included in our study are rat skin and rat-tail tendon. Skin is a clinically relevant sample and rat-tail tendon is analyzed because of its known structure

and availability. Both samples are obtained from a euthanized adult rat. All animals used in this study are cared for according to IACUC guidelines.

Dorsal sections of full-thickness rat skin (approx 4 cm^2 each) are placed in separate glass vials containing either anhydrous glycerol or anhydrous DMSO. An adjacent tissue sample is allowed to dehydrate in air. At nine time points up to 100 hrs samples are weighed and a photographic image is recorded of each sample placed above an opaque ruler functioning as a visible light transmission mask. Samples are epi- and trans-illuminated simultaneously with visible light and photographed using an Olympus C-3040 digital camera. The samples are otherwise kept undisturbed at room temperature.

Individual tail tendon fascicles are imaged with phase contrast microscopy (10X, Ph1 objective) in native and dehydrated states. The native sample is immersed in isotonic saline solution to prevent dehydration. Dehydration stimuli are immersion in anhydrous glycerol and air. The sample immersed in glycerol is imaged after 10 min exposure. The air-dried sample is exposed to air for 30 min and immersed in glycerol immediately prior to imaging. Glycerol immersion provides an index matching media for the bulk fiber, but is too brief to alter scattering properties within the fiber.

Individual tendon fascicles are imaged with an optical coherence tomography (OCT) system operating at 820 nm while exposed to a dehydration stimulus. The first tendon fiber is immersed in glycerol and imaged for 16 minutes. A second tendon fiber is exposed to room air for a period of 2.5 hours. OCT images allow measurement of two dynamic metrics including: 1) cross sectional diameter of tendon fascicle, and 2) intensity of light scattering.

Tissue Ultrastructural Imaging with TEM

The second aim of this paper is to investigate the dehydration mechanism of optical clearing. The first task in completing this aim is inspection of ultrastructure of native and dehydrated tissue (due to both chemically and evaporatively induced dehydration) using transmission electron microscopy (TEM).

Lateral resolution of any light based imaging technique (including OCT) is diffraction limited and unable to reveal structural information of nanometer-sized particles responsible for light scattering. Light scattering structures must be resolved to understand the scattering reduction mechanisms of optical clearing. Therefore, TEM imaging with 5Å resolution was used to reveal the ultra-structural changes in tissue following immersion in a hyperosmotic agent or evaporation.

Samples include both rat-tail tendon fibers and rat hepatocytes. Rat-tail tendon was studied because it is composed of Type I collagen, the primary constituent of human skin (dermis). The advantage of using tendon as an experimental specimen is that collagen fibers are arranged parallel along the tendon axis, unlike the more random fiber orientation in skin. The orderly fiber array facilitates specimen orientation prior to embedding and perimits ultra-sectioning perpendicular to the fiber axis. Hepatocytes are used in lieu of more clinically relevant epidermal keratinocytes because of the difficulty in separating epidermal keratinocytes from dermis. In addition, liver is a homogeneous cellular structure while epidermis is an inhomogeneous cellular structure composed of differentiated keratinocyte layers.

Rat-tail tendon fascicles are cut into 2 cm long sections and liver is cut into $1mm^3$ cubes. Both specimens are immediately submerged into solutions of one of the following hyperosmotic agents: 1) anhydrous glycerol, 2) glycerol in 50% dilution with phosphate buffered saline solution 3) dextrose solution (3 g/ml), or 4) anhydrous DMSO. Agent-treated samples are removed from respective solutions after 20 minutes and excess agent is removed by placing the tissue specimens onto filter paper. Air-dried samples dehydrate in air for 2 hours. All specimens, including a control, are then fixed in 5% gluteraldehyde in Hepes buffer at pH 7.2 for one hour and later embedded in resin according to the following protocol for TEM ultramicrotomy [65].

After primary fixation, the samples are washed three times with HEPES buffer (pH 7.2) solution at 4°C for 1 hour each, with at least one wash held overnight. Buffer washing removes excess gluteraldehyde prior to secondary fixation with buffered 2% osmium tetroxide for 2 hours, followed by three de-ionized water washes of 1 hour each. Fixation minimizes ultrastructural modification that may be induced by necessary subsequent sample preparation dehydration. Tissue dehydration is achieved by ethanol washing in gradually increased ethanol concentrations of 30%, 50%, 75%, and twice with dry absolute ethanol for more than 15 minutes each step. After dehydration of the tissue specimen, propylene oxide is infiltrated as a transitional solvent in three 10-minute changes.

During the final steps of tissue embedding, a medium-hardness formulation of EmBed-812 resin with DMP30 accelerator is gradually added to the samples in propylene oxide until a pure resin mixture is obtained. This process is done over the course of 4

days on a slow tissue rotator in closed glass vials. After the first exchange of 100% EmBed-812, the samples are left overnight on the rotator in opened vials (to evaporate the remaining propylene oxide) and then exchanged with freshly-made resin in BEEM capsules. These are polymerized after 14 hours in a 60°C oven. After trimming and orientation of the fibers in the block by razor blade and glass knives, ultra thin tissue sections are cut 70 to 100 nm thick by a Leica UCT ultramicrotome perpendicularly to the collagen fiber orientation with a Diatome 45 degree diamond knife. Tissue sections are then positively post-stained with uranyl acetate (2% aqueous solution) by placing TEM grids with tissue samples onto a droplet of the stain for 15 minutes.

Stained and unstained tissue sections are imaged with an AMT Advantage HR digital camera at magnifications of up to 28,000x on an FEI EM208 TEM at 80kv. For consistency, images are recorded near the center of each fascicle. Quantitative digital image processing is performed using "ImageJ" software on a SuSE linux computer to obtain cross-sectional area fraction of the fibrils. Area fraction is the ratio of cross-sectional area occupied by fibers to the total image area. One representative image from each experimental trial is analyzed.

Rayleigh-Gans Scattering Predictions

The second part of explaining the dehydration mechanism of tissue optical clearing is relating tissue ultrastructural changes and refractive index changes to alterations in light scattering using the Rayleigh-Gans model. Cell membrane water and glycerol transport was previously investigated in chapter 4 yielding a model relating

dynamic refractive index and volume excursion. This information will be integrated with tissue ultrastructural information gathered from TEM to provide necessary input parameters to the Rayleigh-Gans light scattering model.

Refractive index and cell volume excursion of keratinocytes was previously investigated using DPC-OCM and a cell membrane transport model (chapter 4). This model and the membrane permeability parameters determined in chapter 4 permit investigation of the dynamic excursion of cytosol refractive index and organelle volume fraction for different extracellular osmotic stimuli.

Dynamic excursion of cytosol refractive index and organelle (scatterer) volume fraction combined with cellular ultrastructural information, refractive index of organelles, and several necessary assumptions will provide reasonable input to the Rayleigh-Gans light scattering model. First, a model cell is constructed which satisfies measured and published tissue ultrastructural and refractive index conditions. The Clausius-Masotti relationship between refractive index of a mixture and its constituents is also satisfied for the following conditions [49]. The cytoplasm (n=1.37 [20]) consists of organelles (ϕ=0.25 [62], n=1.42 [22]) and cytosol (ϕ=0.75, n=1.35 [19]). The organelles are composed of water (ϕ=0.14, n=1.33) and dry protein (ϕ=0.11, n=1.54 [66]) and have a radius of 0.5 μm. The cytosol is composed of free water (ϕ=0.58, n=1.33), dry protein (ϕ=0.08, n=1.54), and protein-bound water (ϕ=0.09, n=1.33). The total dry protein volume fraction follows as 0.11+0.08=0.19 which is similar to the protein volume fraction measured in chapter 4. Initial cellular constituent volume fractions are shown in Figure 5.4.

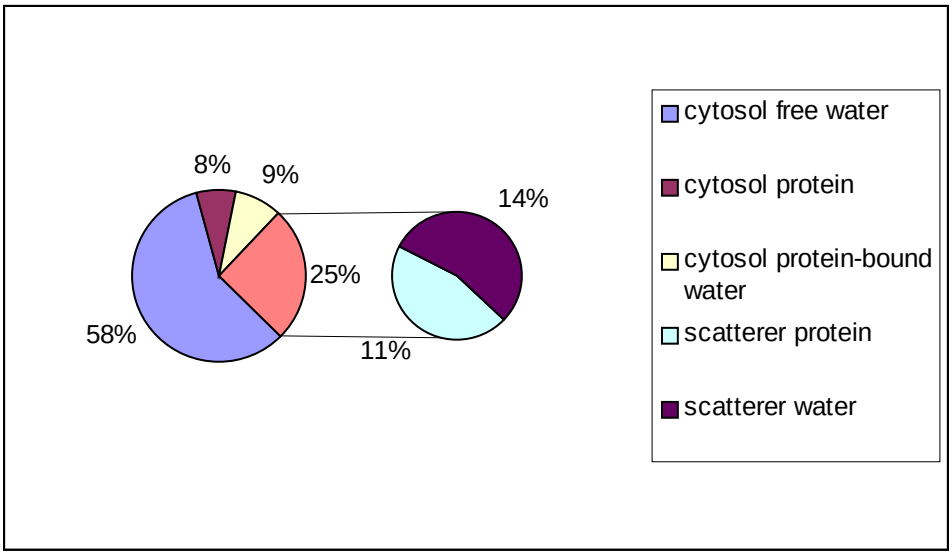

Figure 5.4. Initial cellular constituents and their volume fraction.

Refractive index and size of the organelles is assumed to remain constant during the transient transport process. The only two parameters allowed to dynamically change are the cytosol refractive index and the organelle volume fraction. Organelles and cytosolic protein (with an equal volume of bound water) are impermeable to the cell membrane. As such, the osmotically inactive volume fraction in this model includes the organelles and the cytosolic protein and bound water. The cell membrane hydraulic conductivity and glycerol permeability are 1.31 μm/(min*atm) and 159 μm/min, respectively. The osmotic stimulus investigated is 2.8 M glycerol solution (20% volume).

RESULTS

Optical Clearing Experiment

Optical clearing efficacy is qualitatively assessed by photographic and OCT imaging. Photographic images of rat skin demonstrate various degrees of reduced visible light scattering resulting from exposure to hyperosmotic agents and evaporation (Figure 5.5). Tissue is placed over glass and an opaque ruler and trans- and epi-illuminated. Lighter regions of tissue over the glass and darker regions of tissue over the opaque ruler indicate increased transmission and decreased reflectance, respectively. The DMSO treatment shows very little decrease in native tissue turbidity. Air-drying after 50 hrs clears approximately as well as glycerol.

The ratio of transmittance to reflectance of a tissue qualitatively describes its scattering properties. A high ratio corresponds to low scattering. Transmittance to reflectance ratio (T/R) is quantitatively analyzed for each dehydrated sample by determining the ratio of average intensity of the bottom one-third of each image to the top one-third of each image. T/R is plotted as a function of time and as a function of normalized tissue mass in Figure 5.6.

Tissue mass decreases exponentially versus time for all dehydration stimuli, but the time constant for the dynamic event increases and the equilibrium state decreases for DMSO, glycerol, and air, respectively. T/R for glycerol and air-exposed skin reaches an equilibrium value approximately three times greater than that for DMSO, and the time constant for this dynamic event increases for DMSO, glycerol and air, respectively. Accordingly, T/R is inversely proportional to mass as shown in Figure 5.6c.

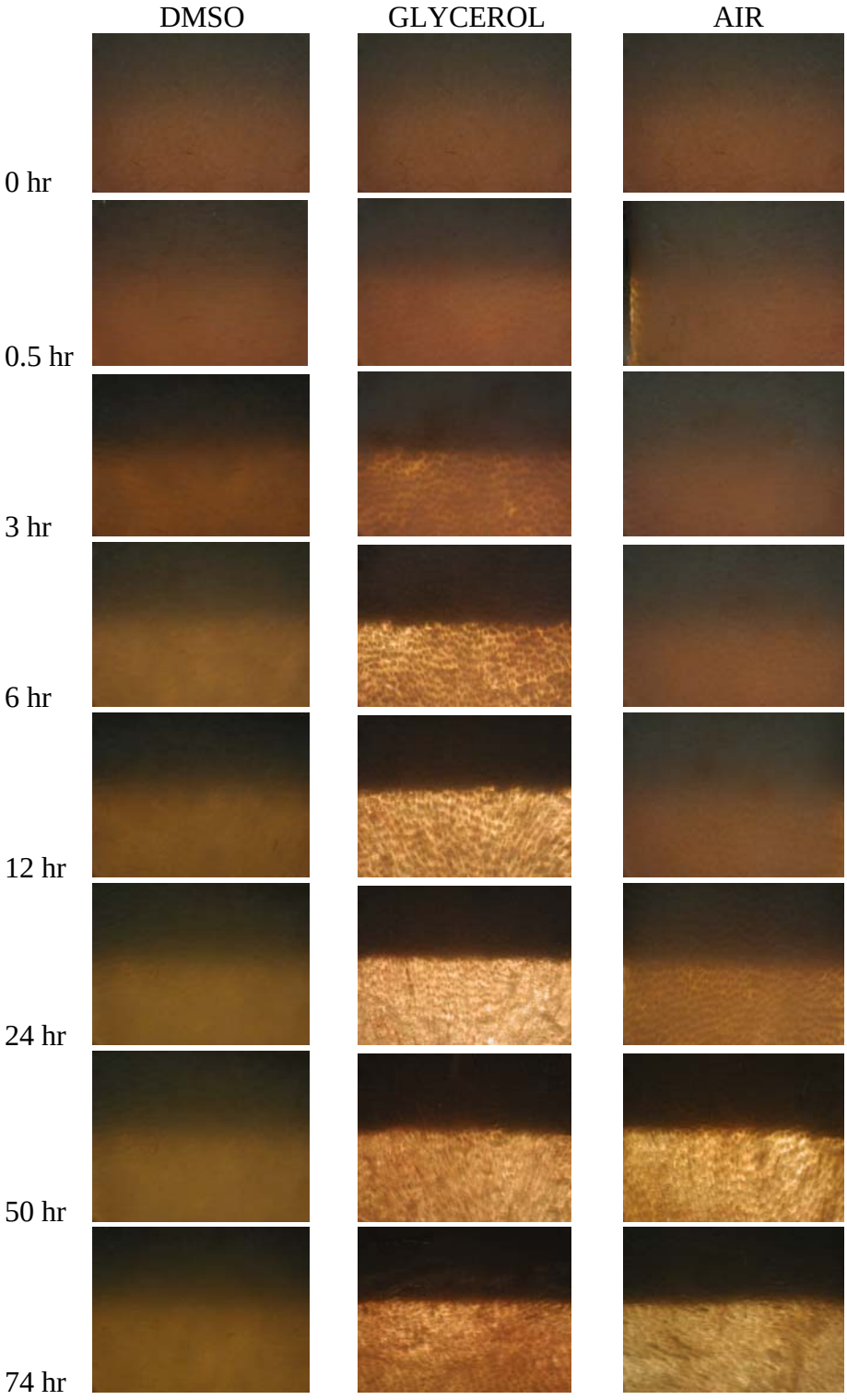

Figure 5.5. Photographic images of rat skin exposed to: DMSO (left column), glycerol (middle column), and air (right column). Corresponding times are listed for each row.

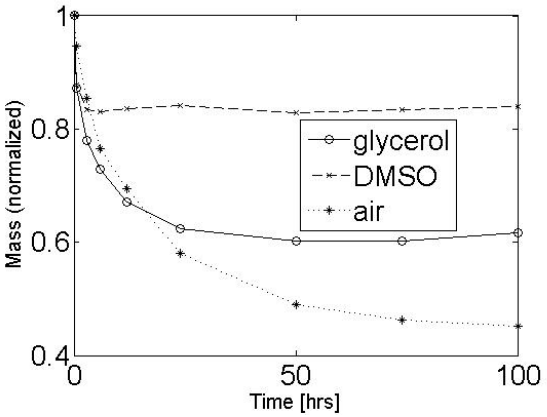

a.

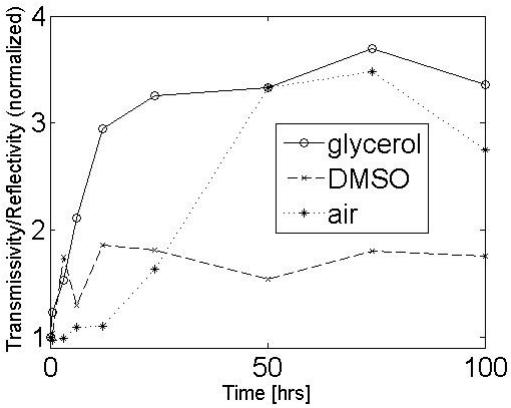

b.

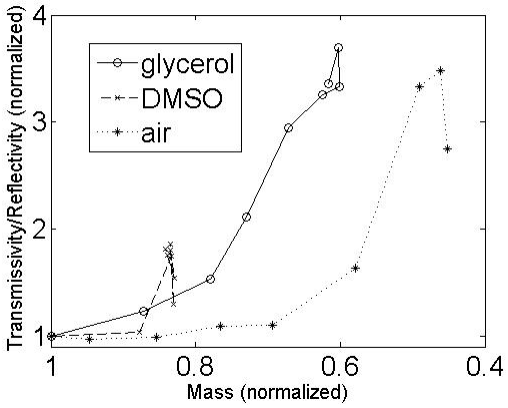

c.

Figure 5.6. a) Normalized dynamic tissue mass. b) Normalized dynamic transmissivity/reflectivity ratio. c) Normalized dynamic transmissivity/reflectivity ratio versus normalized dynamic tissue mass.

Rat-tail tendon exposure to glycerol and dehydration in air causes similar changes in optical properties. Although the tendon fascicle exposed to glycerol optically clears more rapidly than the air-dried sample, at equilibrium they appear equally transparent. See Figure 5.7.

a. b. c.

Figure 5.7. Photographic images of rat-tail tendon a) native, b) glycerol treated for 10 min, c) dehydrated in air for 30 min.

OCT M-scan images of tendon fascicle exposed to glycerol and air are shown in Figure 5.8 a and b. An M-scan is a time sequence of depth scans into tissue at a single lateral position. The x-axis of each image represents time of image acquisition, and y-axis represents scan depth. Back-scattered light intensity [dB] is plotted as a function of time and depth. Initially, after exposure to glycerol or air, backscattered light from the fascicle is large because it is highly turbid. At early times, multiple light scattering is evident as signal in M-scan images from beneath the bottom surface of the tendon. Multiply scattered light undergoes a longer optical path length and is therefore erroneously interpreted as backscattering from a greater depth. Multiple light scattering at early times causes the bottom surface of the tendon fiber to appear blurry and introduces error in the measurement of fiber diameter.

Beneath each M-scan image is corresponding analysis of the dynamic fiber diameter and back-scattered light intensity integrated over the fiber thickness. Glycerol and air exposure cause similar responses in scattering and diameter, although the

response due to glycerol is approximately an order of magnitude faster. The time constant for scattering reduction and fiber shrinkage due to glycerol and air exposure is approximately 2 min and 20 min, respectively. With either dehydration stimulus, scattering increases slightly and then exponentially decays to near 5% of its original value. Similarly, diameter exponentially drops to approximately 75% of its original value, corresponding to a 55% decrease in cross sectional area.

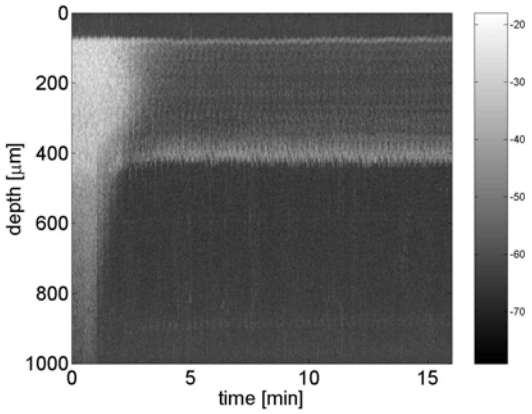

a.

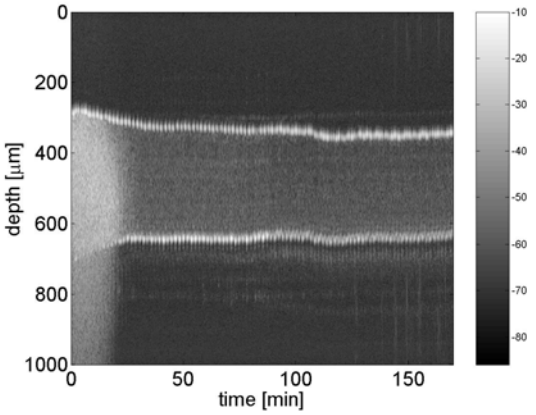

b.

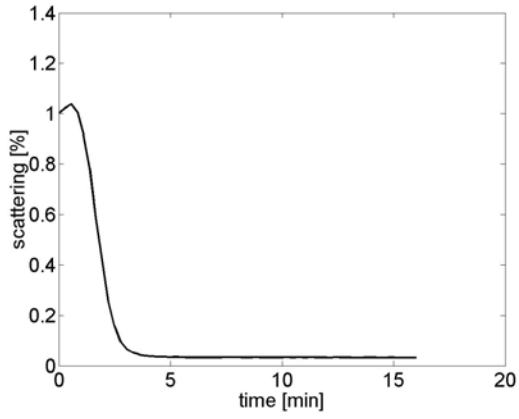

c.

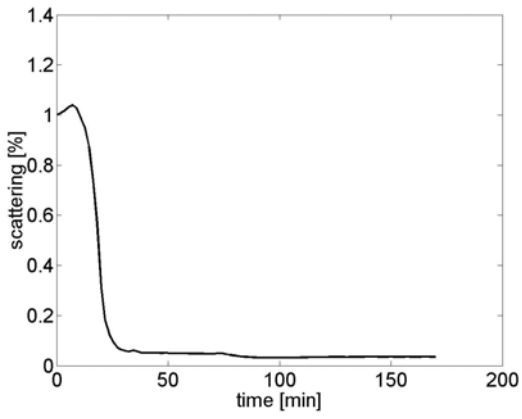

d.

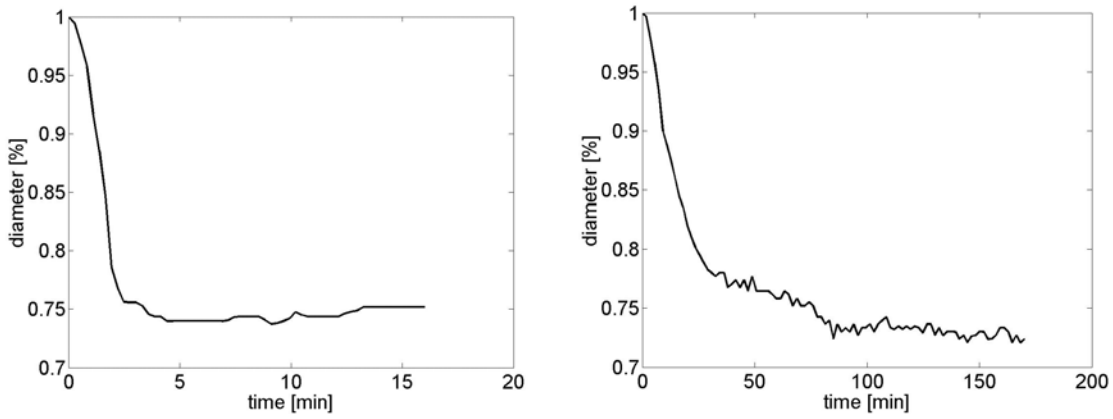

e. f.

Figure 5.8. a) OCT M-scan image (850 nm) of a single rat-tail tendon fiber first exposed to: a) 100% glycerol and b) air. Percentage of original integrated light intensity over fascicle thickness due to exposure to: c) 100% glycerol, and d) air. Cross sectional area change of fascicle due to exposure to: e) 100% glycerol, and f) air.

Tissue Ultrastructural Imaging with TEM

TEM images reveal higher collagen fibril packing densities (area fraction) in the dehydrated tendon samples vs. the native sample. Images of the collagen fibril distribution are shown in Figure 5.9 including: a) native rat-tail tendon fibrils, b) tendon exposed to anhydrous glycerol for 5 minutes, and c) tendon dehydrated in air for 2 hrs. Individual fibrils are easily visible in the native image, but are less discernable in the dehydrated samples. Although a distribution of individual fibril diameters is clearly evident in each image, fibril diameter appears to be relatively unaffected by exposure to

glycerol or air. The largest, approximately 200 nm diameter fibrils account for the majority of the total fibril area fraction.

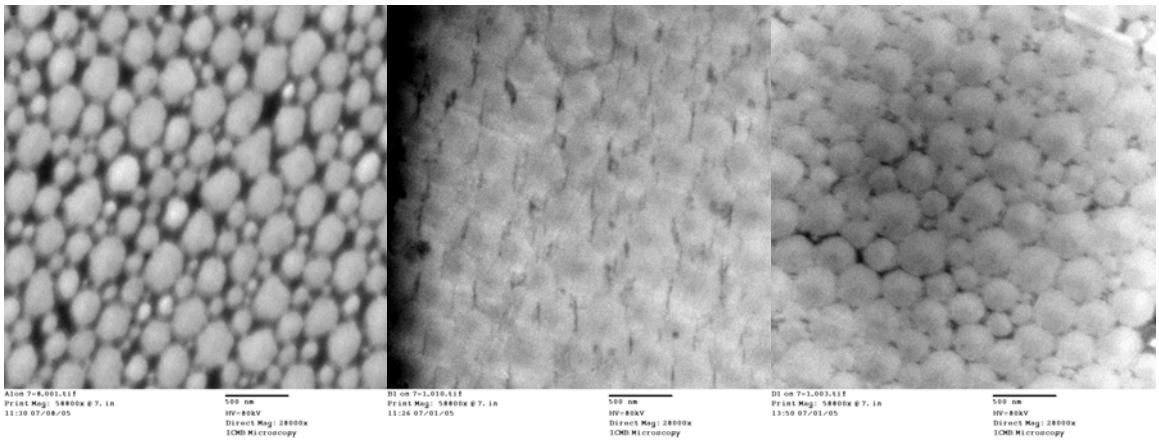

a. b. c.

Figure 5.9. 28,000X TEM images of rat-tail tendon a) native state, b) exposed to anhydrous glycerol for 5 min, and c) dehydrated in air for 2 hrs. Scale bar=500nm.

A quantitative summary of the computational TEM image analysis of tendon samples is shown in Figure 5.10. All dehydrated rat-tail tendon samples show a significant reduction of fibril area fraction. Air-dried tendon causes the greatest increase in packing density. Different hyperosmotic agents cause different degrees of increased fibril area fraction, but all gave at least a 16% increased area fraction compared to native tissue.

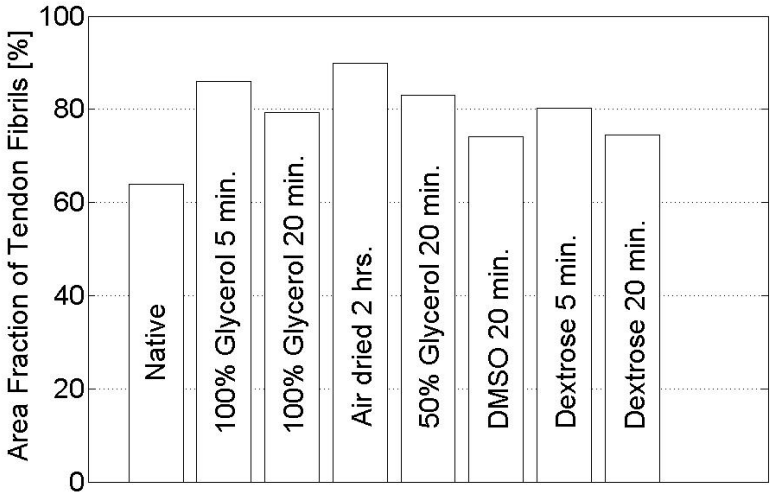

Figure 5.10. Tendon fibril area fraction resulting from exposure to different optical clearing agents.

TEM images of rat hepatocytes reveal higher intracellular organelle packing densities (area fraction) in the dehydrated samples vs. the native sample. Images of the cell in cross-section are shown in Figure 5.11 including: a) native sample, b) sample exposed to glycerol for 10 minutes, and c) sample dehydrated in air for 2 hrs. Individual organelles of different sizes are easily visible in all images. Comparison of glycerol and air-dehydrated samples with the native sample shows noticeably higher organelle packing density. Organelle diameter and area fraction are not quantitatively analyzed.

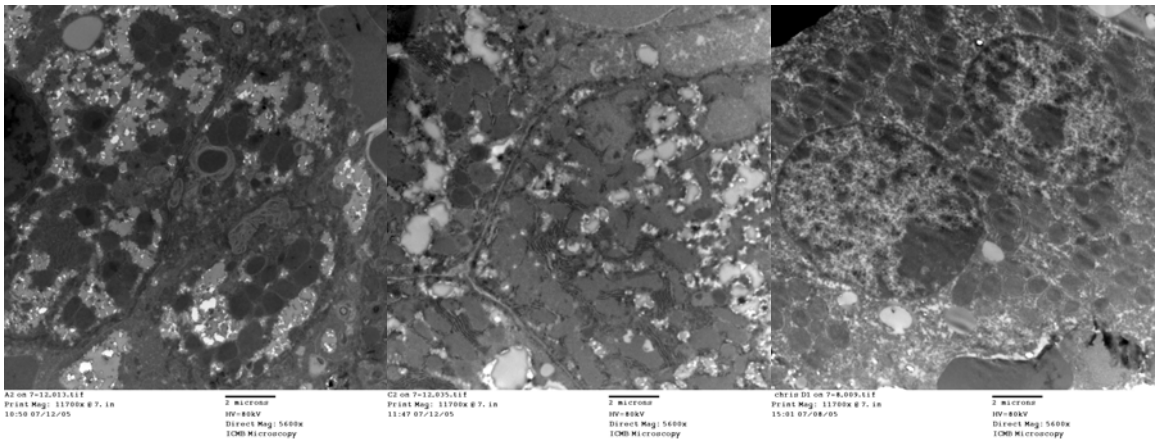

a. b. c.

Figure 5.11. 5600X TEM images of rat hepatocytes a) native, b) dehydrated in glycerol for 10 min, c) dehydrated in air for 4 hrs. Scale bar=2 μm.

Rayleigh-Gans Scattering Simulations

Effects of tendon and cellular ultrastructural changes on reduced scattering coefficient are determined using measured TEM images and the Rayleigh-Gans scattering model. Volume fraction of tendon fibrils and hepatocyte organelles increased from approximately 0.65 to approximately 0.90 due to osmotic and evaporative dehydration while scatterer diameter was unaffected. Assuming the refractive index ratio between fibrils and surrounding fluid remains constant, increased volume fraction corresponds with a 60% decrease in reduced scattering coefficient (Equation 5.2, Figure 5.1).

Using the cell membrane transport model, dynamic excursion of refractive index ratio and scatterer volume fraction are calculated for a 2.8 M glycerol osmotic stimulus. Dynamic refractive index ratio and scatterer volume fraction and their corresponding influence on reduced scattering coefficient are presented in Figure 5.12. Refractive

index ratio decreases substantially from approximately 1.05 to 1.02, effectively reducing scattering. Organelle volume fraction increases minimally from 0.25 to 0.3 for a transient period, minimally increasing scattering. The net effect of these two phenomenon are a substantial and prolonged decrease in reduced scattering coefficient. The result of this experiment indicates refractive index matching due to the presence of glycerol in the cell is the dominant mechanism of cellular optical clearing.

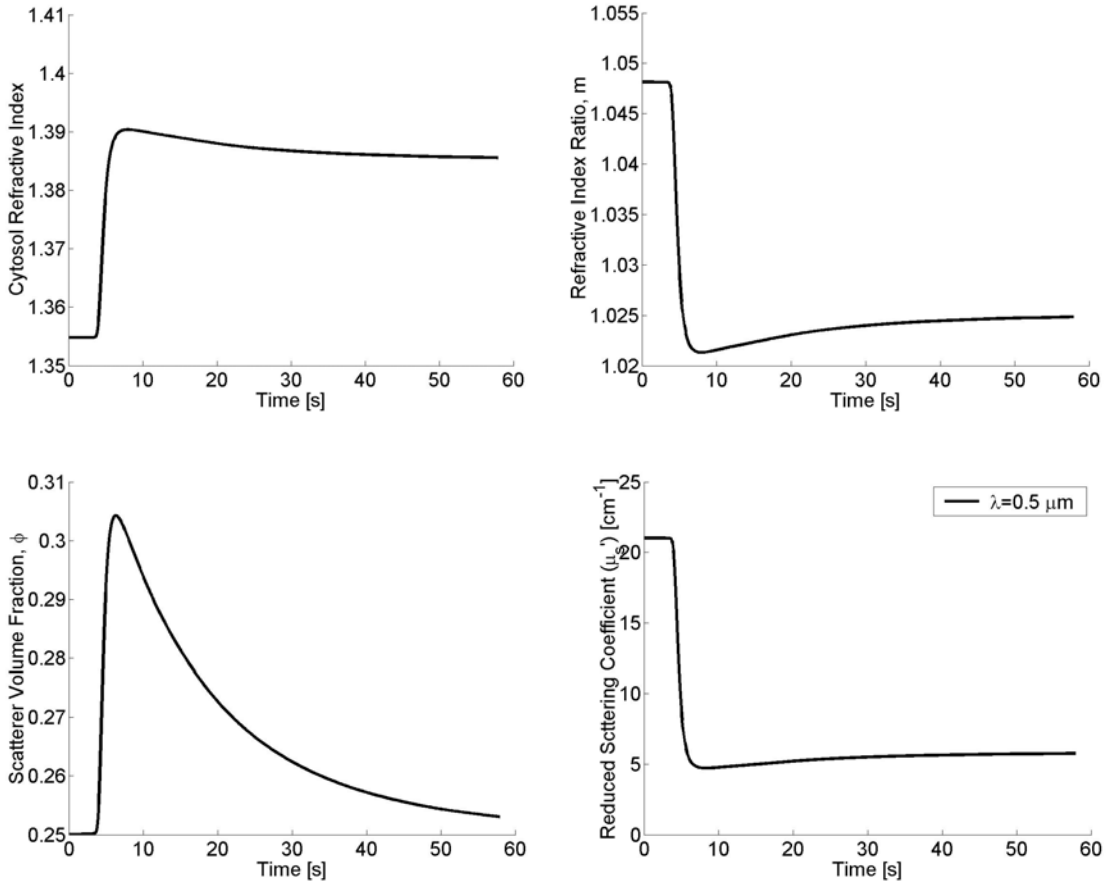

Figure 5.12. a) Dynamic refractive index of cytosol, b) dynamic refractive index ratio, c) dynamic organelle (scatterer) volume fraction, and d) resulting dynamic excursion of reduced scattering coefficient due to the previous parameters.

DISCUSSION

Dehydration induced by evaporation or osmotic stimuli such as hyperosmotic chemical agents appears to be a primary mechanism of optical clearing in collagenous and cellular tissue. Evidence to support this claim includes OCT and photographic images which indicate that air-dried skin and tendon samples are nearly as transparent as their hyperosmotic agent-treated counterparts (Figures 5.5, 5.7, and 5.8). In addition, skin immersed in high refractive index DMSO (n=1.47) does not optically clear as predicted by the hypothesized refractive index matching mechanism.

Optical clearing effectiveness of an individual hyperosmotic agent may be attributed to its ability to dehydrate tissue. For example, glycerol dehydrates and optically clears tissue very successfully while DMSO poorly dehydrates and does not optically clear tissue. Evaporative dehydration dehydrates and optically clears skin as effectively as glycerol, although the process is slower. Refer to Figures 5.5 and 5.6. An explanation for glycerol's ability to dehydrate tissue to a greater extent than DMSO may be its lower permeability. As agent permeability in tissue increases, agent diffusion into tissue may approach the rate of water removal. Once water and agent concentrations within and exterior to the tissue are equal, osmotic driving force is neutralized prior to complete tissue dehydration.

To explain how dehydration causes reduction in light scattering in tissue, we investigate the effects of tissue ultrastructural changes on scattering using the Rayleigh-Gans model. Rayleigh-Gans theory predicts that maximum scattering occurs when volume fraction of scatterers is 0.5 (Equation 5.2, Figure 5.1). As refractive index

matching increases between scatterers and surrounding medium, refractive index ratio, m, approaches unity and Rayleigh-Gans theory predicts scattering to decrease due to reduction of scattering cross section (Equations 5.1 and 5.2). Reduced scattering coefficient is also a function of scatterer radius.

TEM images reveal that dehydration causes individual scatterers (collagen fibrils and organelles) to become more closely packed, but does not cause a noticeable change in scatterer size. Therefore, since native tissue packing density of tendon collagen fibrils and hepatocyte organelles is near 65% and increases to near 90% due to dehydration, Rayleigh-Gans theory predicts this ultrastructural change contributes substantially to optical clearing.

Although we recognize that refractive index-matching occurs as a consequence of dehydration, and the two mechanisms cannot be physically uncoupled, this type of refractive index matching is due to native materials and a passive process, and we wish to differentiate it from index matching due to foreign chemicals such as hyperosmotic agents intentionally introduced to the tissue. The space between fibrils and organelles is occupied by water and suspended proteoglycans. As water is removed from the intra-fibrillar or intracellular space, we expect proteoglycans become more concentrated and refractive index increases. The resulting intrinsic refractive index matching between fibrils or organelles and their surrounding media may significantly contribute to optical clearing.

Investigation of the transient volumetric and refractive index excursion of individual cells to 2.8 M glycerol indicates refractive index matching of glycerol to

cellular organelles is the dominant clearing mechanism. There are several explanations for the apparent discrepancy between this experiment and the TEM images showing very high organelle volume fraction in the glycerol and air immersed specimens. First, high concentrations of glycerol or DMSO (>25% volume) inhibit the Na^+,K^+-ATPase. In the absence of the ion transport pump, water leaks in, causing the cells to swell and eventually lyse [67]. Second, rapid dehydration may cause the cell membrane to lyse and remain fixed in a dehydrated state. Further investigation of the osmotic response of cellular tissue is warranted.

CONCLUSIONS

Dehydration induced by evaporation or osmotic stimuli such as hyperosmotic chemical agents appears to be a primary mechanism of optical clearing in collagenous and cellular tissue. OCT and photographic images indicate that air-dried skin and tendon samples are as transparent as hyperosmotic agent treated samples. In addition, skin immersed in high refractive index DMSO does not optically clear as predicted by the hypothesized refractive index matching mechanism.

TEM images reveal that dehydration causes individual scatterers (collagen fibrils and organelles) to become more closely packed, but does not cause a noticeable change in scatterer size. Rayleigh-Gans theory predicts this ultrastructural change contributes substantially to optical clearing.

ACKNOWLEDGEMENTS

This research was funded by NSF Grant #BES-9986296, NSF IGERT Program, and The Caster Foundation at The University of Texas at Austin.

Chapter 6. Conclusions and Future Directions

CONCLUSIONS

The work contained in this dissertation centered around the application of a differential phase contrast optical coherence microscope to measure the transient transport of hyperosmotic agents across cell membranes and resulting optical clearing. Results of this research include development of a novel quantitative phase contrast microscope which was used to measure cell dry mass and the transport properties of cell membranes. Simulated light scattering effects due to measured dynamic excursions of cellular refractive index and volume were performed using Rayleigh-Gans theory.

In chapter 2 a fiber-based DPC-OCM capable of recording quantitative phase contrast images of individual cells with sub-cellular resolution is demonstrated. A fiber-based DPC-OCM has the potential to substantially improve in vivo imaging of epithelial tissues for a variety of clinical diagnostics and monitoring applications. Results of studies using DPC-OCM to compare normal and cancerous cell populations are presented in chapter 3. Because the DPC-OCM can record transient changes in optical path length, the system may be used to record quantitative optical path length alterations of cells in response to various stimuli. Results of studies of optical path length change of cells in response to a chemical stimulus are discussed in chapter 4.

In chapter 3 DPC-OCM was used to measure *en face* area and dry mass of normal and cancerous populations of human fibroblast and prostate cells. Area and mass population averages are greater in the cancerous versus normal state. There was a significant difference ($p>0.05$) between normal and cancer population averages of dry

mass and area. However, the use of linear discriminant analysis was 75-79% accurate at best. Mass was a better classifier than area for both cell types. It is unlikely that area and mass alone are sufficient parameters to discriminate normal and cancerous cells, however, the combination of these with additional independent experimental parameters may prove an effective discriminant analysis tool.

In chapter 4 a novel approach is presented to determine cell membrane transport properties using optical path length (Φ) images acquired with DPC-OCM and a model relating Φ to the forces and flows that characterize the transport process. Experimental dynamic *en face* cell images provide quantitative data from which physical parameters including intra- and extracellular chemical concentration and transient cell volume may be derived. Hydraulic conductivity, Lp (1.33±1.16 μm/(min*atm)), solute permeability, Ps (163±142 μm/min), and inactive volume fraction, Vb (0.13±0.07) were determined for human keratinocytes (n=16) at 25 ^{o}C. The Φ experimental/modeling technique possesses several salient features over the conventional transport modeling technique. First, the Φ method works for unknown or irregularly shaped cells. Second, the Φ model is capable of simultaneously obtaining the dry mass (protein) of the cell using the principals of immersion refractometry, obviating the need for independent inactive volume fraction measurement using the Boyle-Van't Hoff technique. Third, the extracellular solution concentration in direct contact with an individual cell can be explicitly measured and therefore the conventional assumption of a step change in concentration is not required.

In chapter 5 the prominent role of the dehydration mechanism of tissue optical clearing was presented and explained. Dehydration induced by evaporation or osmotic

stimuli such as hyperosmotic chemical agents appears to be a primary mechanism of optical clearing in collagenous and cellular tissue. OCT and photographic images indicate that air-dried skin and tendon samples are as transparent as hyperosmotic agent treated samples. In addition, skin immersed in high refractive index DMSO does not optically clear as predicted by the hypothesized refractive index matching mechanism. TEM images reveal that dehydration causes individual scatterers (collagen fibrils and organelles) to become more closely packed, but does not cause a noticeable change in scatterer size. Rayleigh-Gans theory predicts this ultrastructural change contributes substantially to optical clearing.

FUTURE DIRECTIONS

Depth-Resolved DPC-OCM for *in-vivo* Cancer Diagnosis

DPC-OCM was successfully applied to measure cell dry mass, a parameter which may be used to differentiate between normal and cancerous populations. Phase-sensitive optical coherence imaging techniques such as DPC-OCM are well suited for tomographich refractive index profiling of tissue. Since refractive index is an intrinsic parameter related to cell dry mass and protein concentration, DPC-OCM may be capable of in-vivo cancer detection. Further studies are warranted.

Cell Membrane Permeability Measurements

Keratinocyte cell membrane permeability parameters to water and glycerol were determined using DPC-OCM and a novel optical path length model. This cell type was selected because of its relevance to optical clearing of skin. Analysis of sixteen experimental samples resulted in a large standard deviation of water and glycerol permeablilty values. The large standard deviation of the experimentally measured parameter values may be attributed to variability in keratinocyte maturation. As keratinocytes mature, they undergo the process of cornification and become less permeable. A suggestion for future experiments is use of a cell type with well-characterized and constant permeability parameters.

Tissue Clearing Mechanisms

Tissue ultrastructural imaging using TEM was performed to better understand the mechanisms of tissue optical clearing. One concern regarding this invaluable data is the degree of ultrastructural modification induced by the required sample preparation technique. Procedures to reduce this undesirable artifact including the "freeze fracture technique" should be investigated for future TEM sample preparation.

More rigorous light scattering modeling techniques, such as the finite difference time domain (FDTD) method, should be investigated to simulate scattering effect due to ultrastructural tissue modification.

Alternative Methods of Tissue Optical Clearing

Based upon a better understanding of the prominent role of the dehydration mechanism of tissue optical clearing, a novel method and device to induce tissue dehydration was invented and a patent has been filed. This method uses mechanical rather than osmotic driving forces to distribute tissue water and other chromophores, thereby engineering the tissue's optical properties. Benefits of this alternative technique include: 1) non-invasive (no chemicals), 2) quick transient response, 3) pain-free, and others. Other means of dehydrating and reducing scattering of tissue should be investigated.

Appendix

Table of Nomenclature (Φ model parameters, description, units, and values)

Parameter symbol		Description	Units	Simulation Values	Inverse Model
n		refractive index of pure species	-		
	nw	refractive index water	-	1.33	1.33
	nper	refractive index permeable solute	-	1.47	1.47
	nimp	refractive index impermeable solute	-	1.54	1.54
	npro	refractive index protein	-	1.54	1.54
Vf^e		volume fraction of extracellular species	-		
	Vf_w^e	volume fraction of extracellular water	-	0.9962 to 0.7981	0.9962 to 0.7981
	Vf_{per}^e	volume fraction of extracellular permeable solute	-	0 to 0.1981	1 to 0.1981
	Vf_{imp}^e	volume fraction of extracellular impermeable solute	-	0.0038	0.0038
	Vf_{pro}^e	volume fraction of extracellular protein	-	0	0
$\tilde{V}$		partial molar volume of species	um^3/mol		
	$\tilde{V}_w$	partial molar volume of water	um^3/mol	1.80E+13	1.80E+13
	$\tilde{V}_{per}$	partial molar volume of permeable solute	um^3/mol	7.10E+13	7.10E+13
	$\tilde{V}_{imp}$	partial molar volume of impermeable solute	um^3/mol	2.70E+13	2.70E+13
	$\tilde{V}_{pro}$	partial molar volume of protein	um^3/mol	7.50E+16	7.50E+16
M^e		molarity of extracellular species	mol/um^3		
	M_w^e	molarity of extracellular water	mol/um^3	calculated	calculated
	M_{per}^e	molarity of extracellular permeable solute	mol/um^3	calculated	calculated
	M_{imp}^e	molarity of extracellular impermeable solute	mol/um^3	calculated	calculated
	M_{pro}^e	molarity of extracellular protein	mol/um^3	calculated	calculated
Vf^i		intracellular volume fraction	-		
	Vf_w^i	intracellular volume fraction of water	-	calculated	calculated
	Vf_{per}^i	intracellular volume fraction of permeable solute	-	0	0
	Vf_{imp}^i	intracellular volume fraction of impermeable solute	-	calculated	calculated
	Vf_{pro}^i	intracellular volume fraction of protein	-	Vb	Vb
M^i		molarity of intracellular species	mol/um^3		
	M_w^i	molarity of intracellular water	mol/um^3	calculated	calculated
	M_{per}^i	molarity of intracellular permeable solute	mol/um^3	calculated	calculated
	M_{imp}^i	molarity of intracellular impermeable solute	mol/um^3	calculated	calculated
	M_{pro}^i	molarity of intracellular protein	mol/um^3	calculated	calculated
N^i		moles of intracellular species	moles		
	N_w^i	moles of intracellular water	moles	calculated	calculated
	N_{per}^i	moles of intracellular permeable solute	moles	calculated	calculated
	N_{imp}^i	moles of intracellular impermeable solute	moles	calculated	calculated
	N_{pro}^i	moles of intracellular protein	moles	calculated	calculated
V^i		volume of intracellular species	um^3		
	V_w^i	volume of intracellular water	um^3	calculated	calculated
	V_{per}^i	volume of intracellular permeable solute	um^3	calculated	calculated
	V_{imp}^i	volume of intracellular impermeable solute	um^3	calculated	calculated

	V_{pro}^{i}	volume of intracellular protein	um^3	calculated	calculated
V_{tot}^{i}		total cell volume	um^3	calculated	calculated
A		cell surface area	um^3	calculated	static input
R		universal gas constant	um^3atm/(mol*K)	8.2x10^13	8.2x10^13
T		absolute temperature	K	295	295
n^{i}		intracellular refractive index	-	calculated	calculated
Φin		intracellular optical path length	um	calculated	dynamic input
n^{e}		extracellular refractive index	-	calculated	calculated
Φex		extracellular optical path length	um	dynamic input	dynamic input
ΔΦ		differential optical path length	um	calculated	calculated
dVw		differential change in intracellular volume of water	um^3	calculated	calculated
dNper		differential change in intracellular moles of permeable solute	moles	calculated	calculated
dNw		differential change in intracellular moles of water	moles	calculated	calculated
dVper		differential change in intracellular volume of permeable solute	um^3	calculated	calculated
t_ch		perfusion chamber thickness	um	calculated	calculated
Lp		hydraulic conductivity (water permeability)	um/(min*atm)	0.1 or 1	calculated
Ps		solute permeability	um/min	10 or 100	calculated
Vb		osmotically inactive volume fraction	-	0.1 or 0.3	calculated

References

1. Vargas G, EK Chan, JK Barton, HG Rylander III, AJ Welch, Use of an agent to reduce scattering in skin, *Lasers Surg Med* 24: 133-141, 1999.
2. Vargas G, "Reduction of light scattering in biological tissue: implications for optical diagnostic and therapeutics, " Doctoral Dissertation, The University of Texas at Austin, Austin, TX, 2001.
3. Vargas G, KF Chan, SL Thomas, AJ Welch, Use of osmotically active agents to alter optical properties of tissue. *Lasers Surg Med* 29: 213-220, 2001.
4. Tuchin VV, IL Maksimova, DA Zimnyakov, IL Kon, AH Mavlutov, AA Mishin, Light propagation in tissue with controlled optical properties, *J Biomed Optics* 2(4): 401-417, 1997.
5. Wang RK, X Xu, VV Tuchin, JB Elder, Concurrent enhancement of imaging depth and contrast for Optical Coherence Tomography by hyper-osmotic agents, *J Opt Sco Am B* 18(7): 948-953, 2001.
6. Anderson RR, JA Parrish, The optics of human skin, *Investigative Dermatology* 77: 13-19, 1981.
7. Yeh AT, B Choi, JS Nelson, BJ Tromberg, Reversible dissociation of collagen in tissues, *J Investigative Dermatology* 121(6): 1332-1335, 2003.
8. Davies HG, MHF Wilkins, The use of the interference microscope to determine dry mass in living cells and as a quantitative cytochemical method, *Quart J Microscopical Sci* 95(3): 271-304, 1954.

9. Mellors RC, J Hlinka, A Kupfer, K Sugiura, Quantitative Cytology and Cytopathology: II. The Quantity of nucleic acid in individual nuclei of normal and neoplastic tissues of the mouse, *Cancer* 7(4): 779-800, 1954.
10. Young D, CA Glasbey, AJ Gray, NJ Martin, Towards automatic cell identification in DIC microscopy, *Royal Microscopical Society* 192: 186-193, 1998.
11. Christensen HN, "Biological transport," WA Benjamin, Inc.: Reading, MA, 1975.
12. House CR, "Water transport in cells and tissues," Edward Arnold Publishers: London, 1974.
13. Pfeffer W, "Osmotic investigations: studies on cell mechanics," Van Nostrand Reinhold: New York, 1985.
14. Stein WD, "Transport and Diffusion Across Cell Membranes," Academic Press Inc.: New York, 1986.
15. Krishna V, CH Fan, JP Longtin, Real-time precision concentration measurement for flowing liquid solutions, *Rev Sci Instruments* 71(10): 3864-3868, 2000.
16. Born M, E Wolf, "Principles of optics," Pergamon Press: New York, 1965.
17. Cuypers PA, JW Corsel, MP Janssen, JMM Kop, WTh Hermens, HC Hemker, *J Biol Chem* 258: 2426, 1983.
18. Barer R, S Joseph, Refractometry of living cells: Part I. Basic Principles, *Quart J Microscopical Sci* 95(4): 399-423, 1954.

19. Maier J, S Walker, S Fantini, M Franceschini, E Gratton, Possible correlation between blood glucose concentration and the reduced scattering coefficient of tissues in the near infrared, *Opt Letters* 19: 2062-2064, 1994.

20. Barer R, Determination of dry mass, thickness, solid and water concentration in living cells, *Nature* 172(4389): 1097-1098, 1953.

21. Barer R, DAT Dick, Interferometry and refractometry of cells in tissue culture, *Exp Cell Res* 4: 103-135, 1957.

22. Beuavoit B, T Kitai, B Chance, Contribution of the mitochondrial compartment to the optical properties of the rat liver: a theoretical and practical approach, *Biophys J*, 67:2501-2510, 1994.

23. *Mosby's Medical Dictionary*, 5th Edition, Anderson K.N., Anderson L.E., Glanze W.D., editors. Mosby-Year Book, Inc. St. Louis, 1998.

24. Odland G.F. Structure of skin. In: Goldsmith L.A., editor. *Physiology, biochemistry and molecular biology of the skin*. New York : Oxford University Press, p. 3-62, 1991.

25. Netter F.H., *Atlas of Human Anatomy*, 2nd Edition, Dalley A.F.II, editor, Novartis, East Hanover, Plate 511, 1997.

26. E. B. Van Munster, L. J. Van Vliet, and J. A. Aten, "Reconstruction of optical path length distributions from images obtained by a wide-field differential interference contrast microscope", Journal of Microscopy, 188, 149 (1997).

27. A. Barty, K. A. Nugent, A. Roberts, and D. Paganin, "Quantitative phase tomography", Optics Communications, 175, 329 (2000)

28. E. Cuche, F. Bevilacqua, and C. Despeursinge, “Digital holography for quantitative phase-contrast imaging”, Optics Letters, 24, 291 (1994).
29. C. Yang, A. Wax, I. Georgakoudi, E. B. Hanlon, K. Badizadegan, R. R. Dasari, and M. S. Feld, “Interferometric phase-dispersion microscopy”, Optics Lett, 25, 1526 (2000).
30. C. Yang, A. Wax, R. R. Dasari, and M. S. Feld, “Phase-dispersion optical tomography”, Optics Letters**,** 26, 686 (2001).
31. M. Sticker, M. Pircher, E. Gotzinger, H. Sattmann, A. F. Fercher, and C. K. Hitzenberger, “*En face* imaging of single cell layers by differential phase-contrast optical coherence microscopy”, Optics Letters, 27, 1126 (2002).
32. C. K. Hitzenberger and A. F. Fercher, “Differential phase-contrast optical coherence tomography”, Optics Letters, 24, 622 (1999).
33. D. P. Davé and T. E. Milner, “Optical low-coherence reflectometer for differential phase measurement”, Optics. Letters, 25, 227 (2000).
34. D. P. Davé, T. Akkin, T. E. Milner, and H. Grady Rylander III, “Phase-sensitive frequency-multiplexed optical low-coherence reflectometry”, Optics. Communications, 193, 39-43 (2001).
35. Zink D, AH Fischer, JA Nickerson, *Nuclear structure in cancer cells*, *Nat. Rev. Cancer* 4, 677-87, 2004.
36. Sandritter W, *Advantages and disadvantages of the interference microscopic procedure in exfoliative cytology*.

37. Barer R, S Joseph, Interference microscopy and mass determination, *Nature* 169: 366-367, 1952.

38. Davé DP, TE Milner, Optical low coherence reflectometer, *Opt Letters* 25(4): 227-230, 2000.

39. Rylander C, DP Davé, T Akkin, TE Milner, KR Diller, and AJ Welch, "Quantitative phase-contrast imaging of cells with phase-sensitive optical coherence microscopy," *Opt Letters* 29(13): 1509-1511, 2004.

40. Conover W, *Practical nonparametric statistics*. New York: Wiley, 1980.

41. Hollander M, DA Wolfe, *Nonparametric statistical inference*. New York: Wiley, 1973.

42. Krzanowski W, *Principals of multivariate analysis*, Oxford University Press, 1988.

43. Schmitt, JM, SH Xiang, and KM Yung, "Speckle in Optical Coherence Tomography," *J Biomed Opt* 4(1):95-105, 1999.

44. Kleinhans FW, Membrane permeability modeling: Kedem-Katchalsky *vs* a two parameter formalism, *Cryobiology* 37:271-289, 1989.

45. Nobel PS, The Boyle-Van't Hoff Relation, *J Theor Biol*. 23(3): 375-379, 1969.

46. Vargas G, KF Chan, SL Thomas, AJ Welch, "Use of osmotically active agents to alter optical properties of tissue," *Lasers Surg Med* 29: 213-220, 2001.

47. Welch AJ, O Stumpp, C Rylander, "Creating the invisible man," *Proc. SPIE* vol. 5319, pp. 285-290, July 2004.

48. Rylander CG, TE Milner, KR Diller, AJ Welch, "Mechanisms of optical clearing in cellular tissue," *Proc. SPIE* 2005 [paper number 5695-14]

49. Feynman RP, RB Leighton, M Sands, *The Feynman lectures on physics, vol 2*, Addison-Wesley, Menlo Park, 1964.

50. Rylander C, KR Diller, TE Milner, AJ Welch, Measurement of transient glycerol concentration in individual cells using optical low coherence reflectometry, *Cryobiology* 45: 237-238, 2002.

51. "Product Information Sheet for CRL-2309", American Type Culture Collection, www.atcc.org, 2002.

52. Aggarwal SJ, KR Diller, and CR Baxter, "Hydraulic permeability and activation energy of human keratinocytes at subzero temperatures," *Cryobiology* 25:203-211, 1988.

53. Rowden G, "Ultrastructural studies of keratinized epithelia of the mouse. III. Determination of volumes of nuclei and cytoplasm of cell in murine epidermis," *J. Invest. Dermatol.* 64: 1-3, 1975.

54. Xu X, Cui Z, Urban JP, "Measurement of the chondrocyte membrane permeability to Me_2SO, glycerol, and 1,2-propanediol," *Med Eng Phys*, 25(7), 573-9, 2003.

55. Gao DY, Mazur P, Kleinhans FW, Watson PF, Noiles EE, and Critser JK, "Glycerol permeability of human spermatozoa and its activation energy," *Cryobiology*, 29(6), 657-67, 1992.

56. Steinke JM and AP Shepherd, "Comparison of Mie theory and the light scattering of red blood cell," *Appl. Opt*. 27, 4027-4033 (1988).

57. Beauvoit B, T Kitai, and B Chance, “Contribution of the mitochondrial compartment to the optical properties of the rat liver: A theoretical and practical approach,” *Biophys. J.* 67, 2501-2510 (1994).

58. Liu H, B Beauvoit, B Chance, Dependence of tissue optical properties on solute-induced changes in refractive index and osmolarity, *J Biomed Optics*, 1(2): 200-211, 1996.

59. Graaff R, JG Aarnoudse, JR Zijp, PMA Sloot, FFM de Mul, J Greve, MH Koelink, Reduced light-scattering properties for mixtures of spherical particles: a simple approximation derived from Mie calculations, *Appl Opt* 31(10): 1370-1376, 1992.

60. Bohren CF, and Huffman DR, *Absorption and scattering of light by small particles*, Wiley, New York (1983).

61. Ishimaru A, *Wave propagation and scattering in random media*, Academic Press, San Diego (1978).

62. Alberts B, D Bray, J Lewis, M Raff, K Roberts, JD Watson, *Molecular biology of the cell 3rd ed*, Garland Publishing, New York, 1994.

63. Drezek R, A Dunn, and R Richards-Kortum, "A Pulsed Finite-Difference Time-Domain Method for Calculating Light Scattering from Biological Cells Over Broad Wavelength Ranges." *Optics Express* vol 6, pp 147-152 (2000).

64. Dunn A, R Richards-Kortum, ``Three-Dimensional Computation of Light Scattering From Cells", *IEEE Journal of Special Topics in Quantum Electronics* vol 2, pp 898-905 (1997).

65. Bozzola J, Russell L, *Electron Microscopy 2nd ed.*, Jones and Bartlett, Boston, 1999.

66. Wang X, Milner TE, Change MC, Nelson JS, "Group refractive index measurement of dry and hydrated type I collagen films using optical low-coherence reflectometry, *J. Biomed. Optics*, 1(2), 212-216, 1996.

67. Barnett RE, "The effects of dimethylsulfoxide and glycerol on Na^+,K^+-ATPase and membrane structure," *Cryobiology* 15, 227-229, 1978.

Vita

Christopher Grady Rylander was born in San Antonio, Texas on January 25, 1978, son of H. Grady Rylander III and Margaret Susan Rylander. He was the Salutatorian of Leander High School in 1996. Following graduation, he attended the University of Texas at Austin College of Engineering. He was selected to participate in the Honor's Scholar Program at the University of Texas Applied Research Laboratories during the summer of 1999. He received his bachelor's and master's degrees in mechanical engineering in August 2000 and May 2002 respectively. He began pursuing a PhD in biomedical engineering at the University of Texas in September 2002 and is expecting to receive his degree in August 2005. During his graduate work he served as a teaching assistant for courses entitled Laser Tissue Interaction: Optical and Electric Circuit Theory Laboratory.

Permanent Address: 3355 Lake Austin Blvd. Apt. A, Austin, TX 78703

This dissertation was typed by Christopher Grady Rylander